

This is the peer reviewed version of the following article:

Anomalous High-Temperature Superconductivity in YH₆ / Troyan, Ia; Semenok, Dv; Kvashnin, Ag; Sadakov, Av; Sobolevskiy, Oa; Pudalov, Vm; Ivanova, Ag; Prakapenka, Vb; Greenberg, E; Gavriliuk, Ag; Lyubutin, Is; Struzhkin, Vv; Bergara, A; Errea, I; Bianco, R; Calandra, M; Mauri, F; Monacelli, L; Akashi, R; Oganov, Ar. - In: ADVANCED MATERIALS. - ISSN 0935-9648. - 33:15(2021), pp. 2006832-2006832. [10.1002/adma.202006832]

Terms of use:

The terms and conditions for the reuse of this version of the manuscript are specified in the publishing policy. For all terms of use and more information see the publisher's website.

09/03/2025 03:52

(Article begins on next page)

Anomalous high-temperature superconductivity in YH_6

Ivan A. Troyan,^{1,&} Dmitrii V. Semenov,^{2,&,*} Alexander G. Kvasnin,^{2,&,*} Andrey V. Sadakov,³
Oleg A. Sobolevskiy,³ Vladimir M. Pudalov,³ Anna G. Ivanova,¹ Vitali B. Prakapenka,⁴ Eran Greenberg,⁴
Alexander G. Gavriliuk,^{1,5} Viktor V. Struzhkin,⁶ Aitor Bergara,^{10,11,12} Ion Errea,^{11,12,13} Raffaello Bianco,¹¹
Matteo Calandra,^{14,15,16} Francesco Mauri,^{16,17} Lorenzo Monacelli,^{16,17} Ryosuke Akashi,¹⁸
and Artem R. Oganov^{2,8,9,*}

¹ Shubnikov Institute of Crystallography, Federal Scientific Research Center Crystallography and Photonics, Russian Academy of Sciences, Moscow 119333, 59 Leninskii Prospekt, Russia

² Skolkovo Institute of Science and Technology, Skolkovo Innovation Center, 3 Nobel Street, Moscow 121205, Russia

³ P. N. Lebedev Physical Institute, Russian Academy of Sciences, Moscow 119991, Russia

⁴ Center for Advanced Radiation Sources, The University of Chicago, 5640 South Ellis Avenue, Chicago, Illinois 60637, USA

⁵ IC RAS Institute for Nuclear Research, Russian Academy of Sciences, Moscow, 117312 Russia

⁶ Center for High Pressure Science and Technology Advanced Research, Shanghai 201203, China

⁸ Moscow Institute of Physics and Technology, 9 Institutsky Lane, Dolgoprudny 141700, Russia

⁹ International Center for Materials Discovery, Northwestern Polytechnical University, Xi'an 710072, China

¹⁰ Departamento de Física de la Materia Condensada, University of the Basque Country (UPV/EHU), 48080 Bilbao, Basque Country, Spain

¹¹ Centro de Física de Materiales CFM, CSIC-UPV/EHU, Paseo Manuel de Lardizabal 5, 20018 Donostia, Basque Country, Spain

¹² Donostia International Physics Center (DIPC), Manuel Lardizabal pasealekua 4, 20018 Donostia, Basque Country, Spain

¹³ Fisika Aplikatua 1 Saila, University of the Basque Country (UPV/EHU), Europa Plaza 1, 20018 Donostia, Basque Country, Spain

¹⁴ Dipartimento di Fisica, Università di Trento, Via Sommarive 14, 38123 Povo, Italy

¹⁵ Sorbonne Université, CNRS, Institut des Nanosciences de Paris, UMR7588, F-75252 Paris, France

¹⁶ Graphene Labs, Fondazione Istituto Italiano di Tecnologia, Via Morego, I-16163 Genova, Italy

¹⁷ Dipartimento di Fisica, Università di Roma Sapienza, Piazzale Aldo Moro 5, I-00185 Roma, Italy

¹⁸ University of Tokyo, 7-3-1 Hongo, Bunkyo, Tokyo 113-8654, Japan

Abstract

Pressure-stabilized hydrides are a new rapidly growing class of high-temperature superconductors which is believed to be described within the conventional phonon-mediated mechanism of coupling. Here we report the synthesis of yttrium hexahydride $Im\bar{3}m\text{-YH}_6$ that demonstrates the superconducting transition with $T_C \sim 224$ K at 166 GPa, much lower than the theoretically predicted (>270 K). The measured upper critical magnetic field $B_{c2}(0)$ of YH_6 was found to be 116–158 T, which is 2–2.5 times larger than the calculated value. A pronounced shift of T_C in yttrium deuteride YD_6 with the isotope coefficient 0.4 supports the phonon-assisted superconductivity. Current-voltage measurements showed that the critical current I_C and its density J_C may exceed 1.75 A and 3500 A/mm² at 0 K, respectively, which is comparable with the parameters of commercial superconductors, such as NbTi and YBCO. The superconducting density functional theory (SCDFT) and anharmonic calculations suggest unusually large impact of the Coulomb repulsion in this compound. The results indicate notable departures of the superconducting properties of the discovered YH_6 from the conventional Migdal-Eliashberg and Bardeen–Cooper–Schrieffer theories.

Keywords: yttrium hydrides, superconductivity, USPEX, high pressure, SCDFT, SSCHA

Highlights

- High- T_C superconductivity in $Im\bar{3}m\text{-YH}_6$ at 224 K and 166 Gigapascals
- Upper critical magnetic field of YH_6 is 116–158 Tesla at 0 K
- Critical current density (~ 3500 A/mm²) in yttrium hexahydride may exceed parameters of YBCO and NbTi.
- Notable discrepancies between the T_C and $B_{c2}(0)$ predicted within BCS model, and the experimental values

Introduction

Room-temperature superconductivity has been an unattainable dream and subject of speculative discussions for a long time, but times change. The theoretical prediction of record high-temperature superconductor LaH_{10} ¹ followed by the experimental confirmation of its critical temperature $T_C \sim 250\text{--}260\text{ K}^{2-4}$ has opened a new field in high-pressure physics devoted to the investigation of superconducting metal hydrides. Recent successful synthesis of previously predicted superconducting BaH_{12} ,⁵ ThH_{10} ,⁶ UH_7 and UH_8 ,⁷ CeH_9 ,⁸ PrH_9 ,⁹ and NdH_9 ¹⁰ motivated us to perform an experimental study of the Y–H system to find previously predicted potential room-temperature superconductor $Im\bar{3}m\text{-YH}_6$, stable in pressure range of 110–300 GPa.^{1,11,12}

The outstanding superconducting properties combined with a relatively low predicted stabilization pressure of about 110 GPa¹¹ make yttrium hexahydride very interesting. Starting from 2015, the stability, conditions and physical properties of YH_6 , having a sodalite-like crystal structure similar to another predicted hexahydride $Im\bar{3}m\text{-CaH}_6$, have been studied in several works.^{1,11,12} In 2015, Li et al.¹¹ have predicted the stability of $Im\bar{3}m\text{-YH}_6$ at pressures over 110 GPa. Solving the Migdal–Eliashberg (ME) equations numerically, they found a superconducting transition temperature $T_C = 251\text{--}264\text{ K}$ at 120 GPa ($\mu^* = 0.1\text{--}0.13$), with the electron-phonon coupling (EPC) coefficient λ reaching 2.93. In the study of the physical properties and superconductivity of $Im\bar{3}m\text{-YH}_6$ by Heil et al. in 2019,¹³ the most detailed so far, the calculations were made using the fully anisotropic Migdal–Eliashberg theory (as implemented in the EPW code) with Coulomb corrections. They have found that an almost isotropic superconducting gap in YH_6 is caused by a uniform distribution of the coupling over the states of both Y and H sublattices and have predicted the critical temperature $T_C = 290\text{ K}$ at 300 GPa¹³. A summary of the previous results of theoretical studies of $Im\bar{3}m\text{-YH}_6$ is shown in Supplementary Table S6 and Fig. S11.

Following the theoretical predictions, in this work we report experimental study of the superconducting properties of yttrium hexahydride $Im\bar{3}m\text{-YH}_6$, synthesized together with YH_7 and YH_4 , after laser heating yttrium samples compressed to 166–172 GPa in the ammonia borane (NH_3BH_3) medium in the diamond anvil cells.

Results and discussion

In the first part of this work we focused on the experimental verification of stability and superconductivity of $Im\bar{3}m\text{-YH}_6$ and on the calculation of some physical properties that have not been analyzed before.

The high-pressure synthesis was carried out with ammonia borane as a source of hydrogen, following the technique that has shown good results in previous studies.^{2,3,6,9,10} We prepared three diamond anvil cells (DACs) with 50 μm culets (K1, M1, and M3), where pure yttrium metal was loaded into sublimated ammonia borane and compressed to 166–172 GPa. The pulsed laser heating technique was used to heat samples at 2400 K (10^5 pulses, 1 μs pulse width, 10 kHz) that resulted in the formation of three compounds $Im\bar{3}m\text{-YH}_6$ and YH_4 or YH_{7+x} in all DACs.

The results of the synthesis are strongly dependent on pressure and temperature conditions. In DACs K1 and M1 (the X-ray diffraction (XRD) patterns are shown in Figure 1 and Supplementary Fig. S7 and S8), the laser heating of the samples at 166 GPa yielded a complex mixture of products with predominant $Im\bar{3}m\text{-YH}_6$ and, probably, $P1\text{-YH}_7$ or pseudocubic $Imm2\text{-YH}_7$ (Supplementary Fig. S7), which have been found using the USPEX structure search.^{14–16}

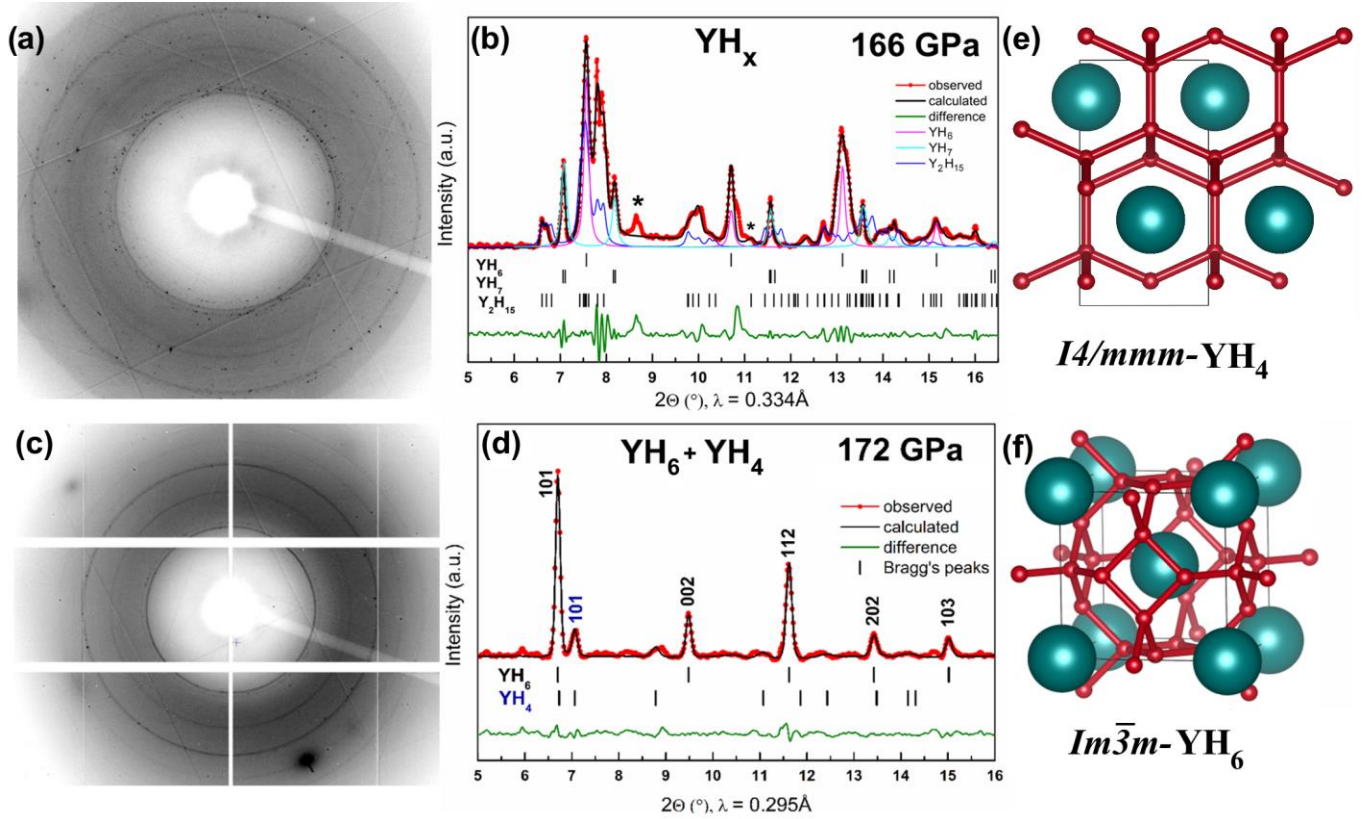


Figure 1. (a) The X-ray diffraction (XRD) pattern of the sample in DAC K1 at 166 GPa collected at a wavelength of $\lambda = 0.3344 \text{ \AA}$. (b) The Le Bail refinements of $Im\bar{3}m\text{-YH}_6$, $Imm2\text{-YH}_7$, and $P1\text{-YH}_{7+x}$ ($x = \pm 0.5$) at 166 GPa. Unidentified reflections are marked by asterisks. (c) XRD pattern of the M3 sample at 172 GPa collected with $\lambda = 0.2952 \text{ \AA}$. (d) The Le Bail refinements of $Im\bar{3}m\text{-YH}_6$ and $I4/mmm\text{-YH}_4$. The experimental data, fitted line, and residues are shown in red, black, and green, respectively. (e-f) Crystal structures of YH_4 and YH_6 .

At higher pressures (172–180 GPa, DAC M3), a much simpler XRD pattern was observed (Figure 1c, d), with peaks only from the $Im\bar{3}m\text{-YH}_6$ and distorted $I4/mmm\text{-YH}_4$ phases. The experimental lattice parameters and volumes of synthesized $Im\bar{3}m\text{-YH}_6$ are given in the Table 1 (for YH_4 and YH_7 , see Supplementary Tables S3 and S5). All Y–H phases were also theoretically examined for the dynamic and mechanical stability according to the Born criteria ($C_{11} - C_{12} > 0$, $C_{11} + 2C_{12} > 0$, $C_{44} > 0$), the obtained results are presented in Supplementary Tables S10–S12.

Table 1. The experimental (a , V) and predicted (a_{DFT} , V_{DFT}) lattice parameters and volumes of $Im\bar{3}m\text{-YH}_6$ ($Z = 2$).

DAC	Pressure, GPa	a , \AA	V , \AA^3	a_{DFT} , \AA	V_{DFT} , \AA^3
M1	166	3.578(3)	45.82	3.573	45.62
K1	168	3.582(3)	45.91	3.565	45.31
M3	172	3.571(2)	45.53	3.557	45.02
M3	177	3.565(9)	45.34	3.551	44.79
M3	180	3.559(8)	45.07	3.546	44.58

To estimate the thermodynamic stability and the possibility of formation of these hydrides at the experimental pressure-temperature conditions, we carried out searches for stable Y–H compounds using the evolutionary algorithm USPEX^{14,15,17} at 150, 200, 250, and 300 GPa. The results of the computational predictions at 0, 500, 1000, and 2000 K (with the zero-point energy (ZPE) included at the harmonic level) and a pressure of 150 GPa are shown in Figure 2 (for other pressures, see Supplementary Fig. S2–S6).

At 150 GPa and 0 K, with the ZPE contribution taken into account, the only stable hydrides are $Fm\bar{3}m$ -YH and YH_3 , $I4/mmm$ -YH₄, $P1$ -YH₇ ($Imm2$ -YH₇ is a bit less stable), and pseudohexagonal $P\bar{1}$ -YH₉, whereas $Im\bar{3}m$ -YH₆ is metastable, lying 30 meV/atom above the convex hull (Figure 2a). The distorted hydrogen sublattice in $P\bar{1}$ -YH₉ leads to a lower enthalpy of formation compared with previously proposed $P6_3/mmc$ -YH₉,¹⁸ which has an ideal hexagonal structure (Supplementary Fig. S1). The cubic modification of YH₉ with space group $F\bar{4}3m$ (isostructural with PrH₉)⁹ is more stable than $P6_3/mmc$ -YH₉¹⁸ (Figure 2a).

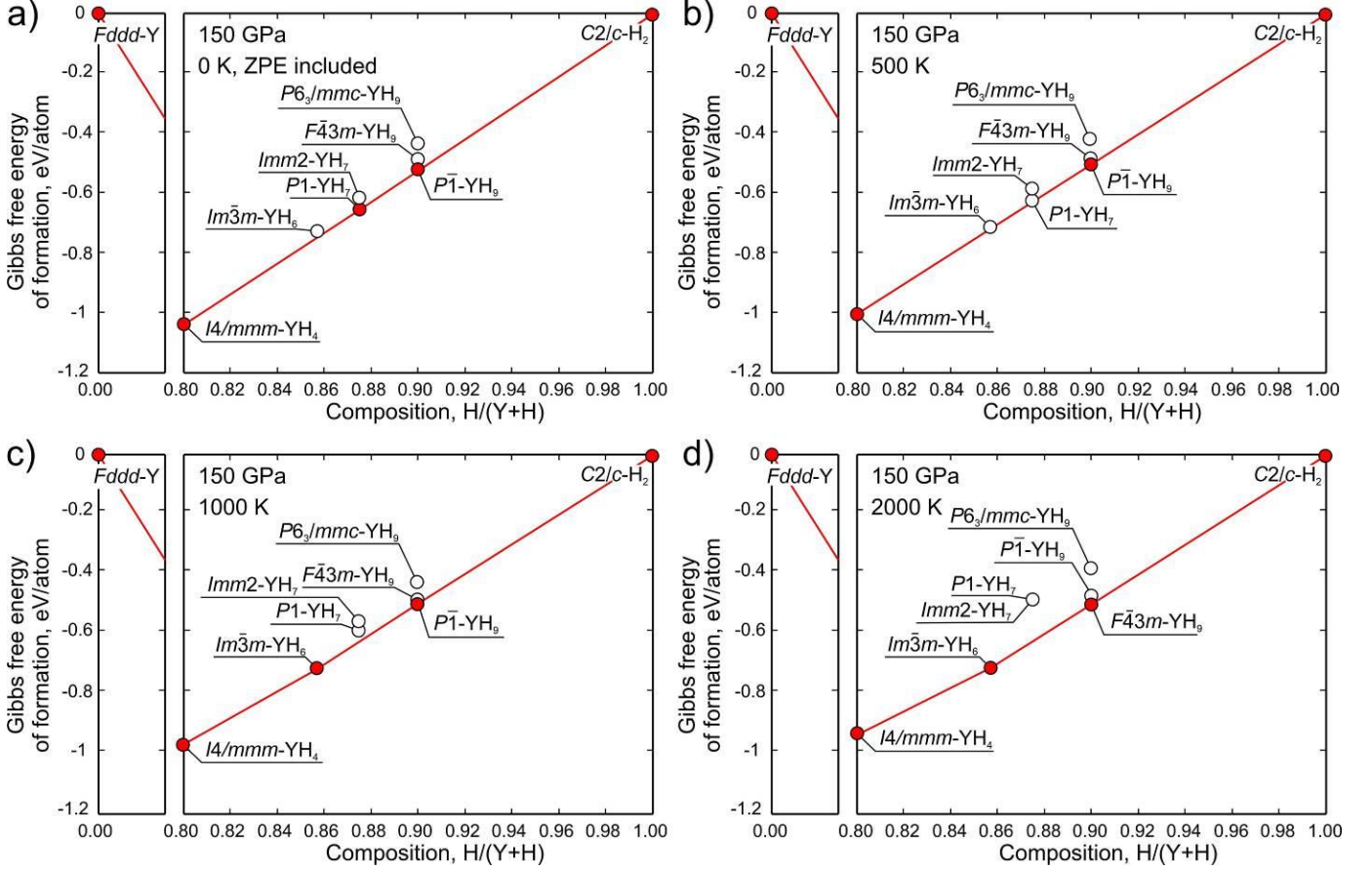


Figure 2. Calculated convex hulls of the Y–H system at 150 GPa and (a) 0 K, (b) 500 K, (c) 1000 K, and (d) 2000 K.

As the temperature rises, the separation of the YH₇ from the convex hull also increases to 110 meV/atom at 2000 K (Figure 2d). Laser heating of the samples above 1000 K (Figure 2c) leads to the stabilization of $Im\bar{3}m$ -YH₆ and transformation of the pseudohexagonal $P\bar{1}$ -YH₉ to the cubic modification of YH₉, which becomes stable at temperatures above 1500 K (Figure 2d). Calculations at 200 and 250 GPa (Supplementary Fig. S5 and S6) show that both $P1$ -YH₇ and $Im\bar{3}m$ -YH₆, which below 150 GPa is a metastable “frozen” phase, can form simultaneously, in accordance with the experimental data. In contrast to early predictions^{1,11,12}, our computations, considering $P1$ -YH₇ and $P\bar{1}$ -YH₉, show that yttrium hexahydride stabilizes at 100–150 GPa only due to the entropy factor.

It is interesting that $Fm\bar{3}m$ -YH₁₀ is thermodynamically metastable at 200–250 GPa and 0–2000 K, with the Gibbs free energy of formation at least 18 meV/atom above the convex hull because of the existence of YH₉ (Supplementary Figure 25 and S6). This may explain the failure to synthesize $Fm\bar{3}m$ -YH₁₀ at 243 GPa.¹⁸ On the other hand, the stabilization of $F\bar{4}3m$ -YH₉ may shed light on the recent detection of superconductivity in YH_x at 262 K by the group of Ranga Dias.¹⁹

To measure the superconducting transition temperature of synthesized yttrium hexahydride, all DACs were equipped with four Ta/Au electrodes. We used the DACs with a 50 μm culet bevelled to 300 μm at 8.5°. Four Ta electrodes (~200 nm thick) with a gold plating (~80 nm) were sputtered on the diamond anvil.

The composite gaskets consisting of a tungsten ring and a CaF₂/epoxy mixture were used to isolate the electrical leads. To measure the isotope effect in YD₆, a similar cell loaded with ND₃BD₃ was prepared.

An yttrium sample with a thickness of ~1–2 μm was sandwiched between the electrodes and ammonia borane in the gasket hole with a diameter of 20 μm. In the DAC M3, the electrodes were in short-circuit with the tungsten gasket, therefore no resistivity measurements were made. The temperature dependence of the resistance is shown in Figure 3. In each cooling cycle, the pressure increased because of the thermal expansion of the DAC materials.

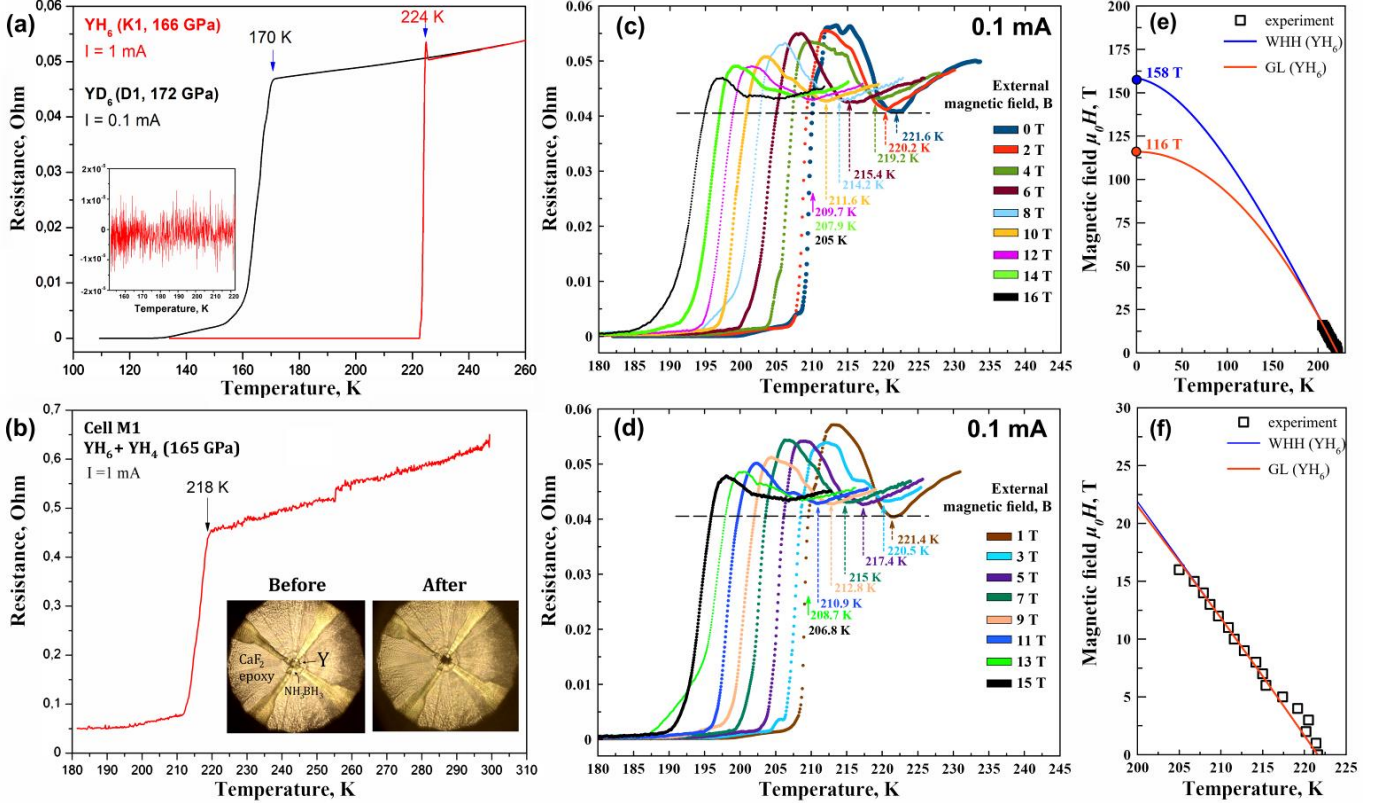


Figure 3. Superconducting transitions in the $Im\bar{3}m$ -YH₆: (a) the temperature dependence of the electrical resistance $R(T)$ in the YH₆ (DAC K1) and YD₆ (DAC D1). Inset: the resistance drops to zero after cooling below T_C ; (b) temperature dependence of the electrical resistance in DAC M1. A 9-fold decrease is observed; (c, d) dependence of the electrical resistance on the external magnetic field (0–16 T) at 183 GPa and a current of 0.1 mA for (c) even and (d) odd values of the magnetic field. Due to presence several hydride phases in the sample the superconducting transition in YH₆ can be observed as an upward feature of the $R(T,H)$ curves due to the shunting effect in the fine-grained samples. The critical temperatures were determined at the onset of the resistance jump; (e) the upper critical magnetic field estimated using the Werthamer–Helfand–Hohenberg theory²⁰ and the Ginzburg–Landau²¹ theory; (f) the dependence of the critical temperature T_C (YH₆) on the applied magnetic field.

Two slightly different superconducting transitions in the YH₆ with T_C of 224 K (Figure 3a) and 218 K (Figure 3b) were observed in the DACs K1 and M1, respectively. In the K1 cell, the electrical resistance dropped sharply to zero (from 50 mΩ to 5 μΩ, with $\Delta T_C \sim 1$ –2 K) due to good location of the sample, whereas in the M1 cell the electrical resistance did not disappear completely because of the presence of additional phases (Supplementary Fig. S7). The YD₆ sample synthesized using deuterated ammonium borane demonstrates superconducting transition at 170 K, which corresponds to the isotope coefficient $\alpha_{\text{exp}} = 0.4$, lower than the BCS theory gives (~0.5).

The analysis of the electronic and superconducting properties of the tetragonal YH₄ and pseudocubic $Imm2$ -YH₇ shows that the $I4/mmm$ -YH₄ is a metal with a significantly lower calculated critical temperature (≤ 94 K) compared with YH₆. Another possible product of the synthesis in DAC M1, $Imm2$ -YH₇, has a

pronounced pseudogap in the electronic density of states $N(E)$, leading to a quite low density of states at the Fermi level $N(E_F)$, and, as a result, low predicted T_C of 32–43 K (Supplementary Table S7, Fig. S14). Other possible crystal modifications of YH_7 , such as Cc or $P1$, have even lower $N(E_F)$ and T_C . Thus, the presence of these phases has practically no effect on the superconducting transition in the yttrium hexahydride.

In YH_6 , the dependence of the T_C (YH_6) on the magnetic induction $B = \mu_0 H$ was measured at 183 GPa in the range of 0–16 T (Figure 3c, d) and interpolated using the Ginzburg–Landau²¹ and the Werthamer–Helfand–Hohenberg (WHH)²⁰ models simplified by Baumgartner.²² Around 200 K, an almost linear dependence of the $T_C(B)$ with a gradient $dB_{c2}/dT \approx -1$ T/K was observed (Figure 3f). The experimentally found upper critical field $\mu_0 H_{c2}(0)$ for YH_6 is 116–158 T, in agreement with the results of Kong et al.¹⁸ These data allows us to estimate $N(E_F)(1 + \lambda)$ factor in the interpolation formula proposed by Carbotte²³ for the $B_{c2}(0)$ of conventional superconductors (Supplementary Table S7) at 7.2–13.3 eV⁻¹f.u.⁻¹.

One of distinguishing features of superconductors is the existence of an upper limit of the current density (J_C) at which superconductivity disappears. The critical currents and the voltage–current (V–I) characteristics for the YH_6 sample were investigated in the range of 10^{-4} – 10^{-2} A in external magnetic fields after further compression to 196 GPa (Figure 4a, b). The critical current density was estimated on the basis of the facts that the size of the sample cannot exceed the size of the culet (50 μm), and the thickness of the sample is smaller than the thickness of the gasket before the cell is loaded, ~ 10 μm . A zero-field cooling (ZFC) shows that the critical current density in YH_6 exceeds 2×10^7 A/m² at $T = 190$ K. To compare critical currents in magnetic fields at low temperatures we used a single vortex model. Critical current density in magnetic fields may be defined as the current that creates strong enough force to de-pin a vortex or a bundle of vortices. There are two possible sources of pinning: non-superconducting (normal) particles embedded in the superconducting matrix leading to a scattering of electrons, so called "dl-pinning", or pinning provided by spatial variations of the Ginzburg parameter ($\kappa = \lambda/\xi$) associated with fluctuations in the transition temperature T_C , so called "dT_C-pinning" (or dk-pinning).

Analysis of the pinning force ($F_p = B \cdot J_C$) dependence on magnetic field (Supplementary Fig. S13a) shows that according to Dew-Hughes²⁴ the dominant type of pinning in YH_6 is "dl-pinning". This allows us to extrapolate $I_C(T)$ data to low temperatures within the single vortex model $J_C = J_{c0}(1 - T/T_C)^{5/2}(1 + T/T_C)^{-1/2}$ which is suitable for rather low fields of several Tesla in the whole temperature range (see equation (8) in Ref. ²⁵). The extrapolation shows that at 4.2 K the critical current I_C in the sample can reach 1.75 A and the critical current density J_C may exceed 3500 A/mm² (Figure 4c). However, using the Ginzburg–Landau model,²¹ $J_C = J_{c0}(1 - T/T_C)^{3/2}$, gives lower values: the maximum critical current I_C in the sample ~ 1 A, and the maximum critical current density J_C is about 2000 A/mm² (Supplementary Fig. S13b). These values of J_C are comparable with the parameters of commercial superconducting materials like NbTi and YBCO²⁶ (Figure 4d), which opens prospects of using superhydrides in electronic devices.

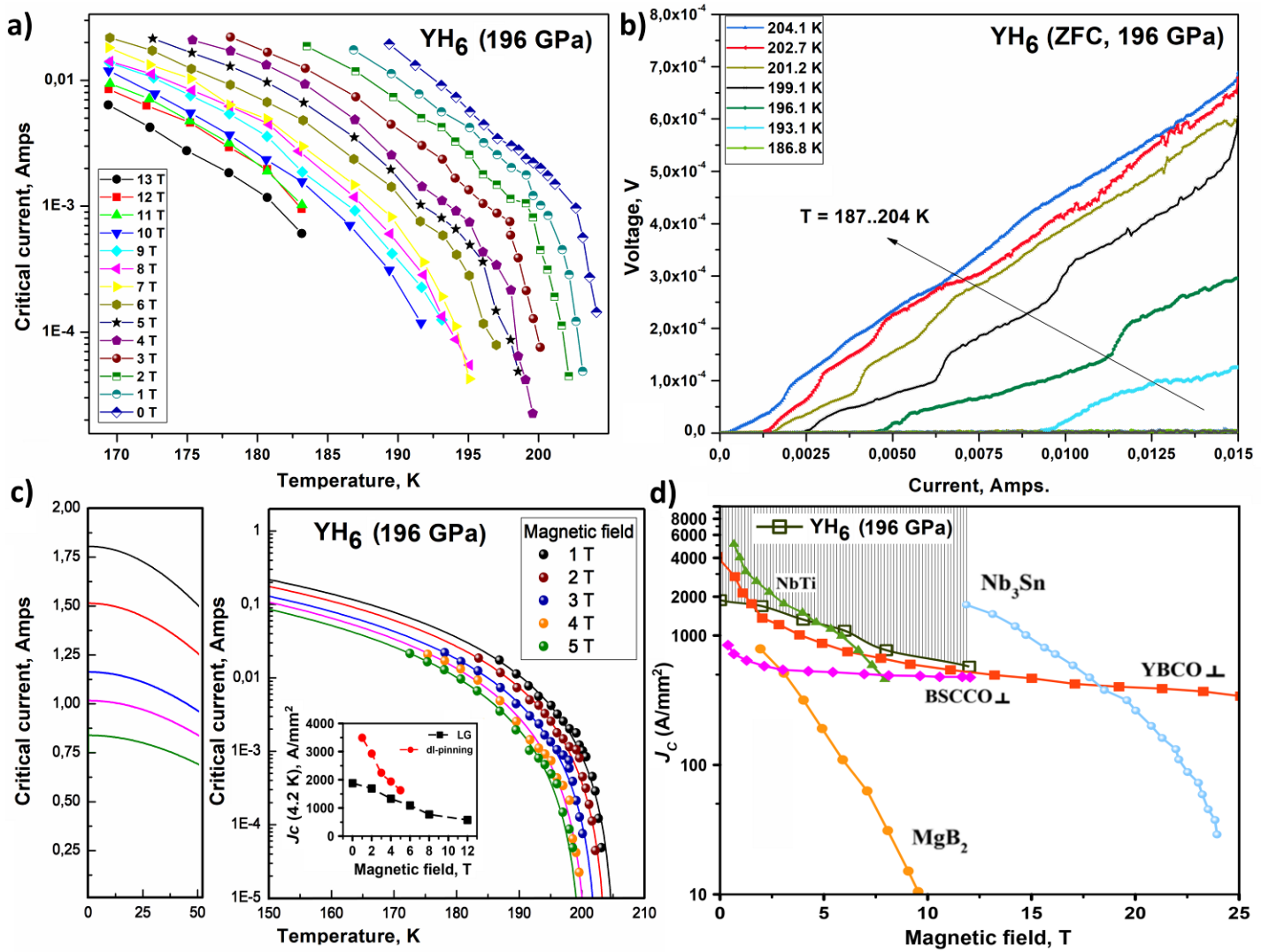


Figure 4. Dependence of the critical current on the temperature and external magnetic fields (0–13 T) in $Im\bar{3}m$ -YH₆ at 196 GPa. (a) The critical current at different magnetic fields near T_C (defined below 50% resistance drop). (b) The voltage–current characteristics of the YH₆ sample near T_C . (c) Extrapolation of the temperature dependence of the critical current using the single vortex model²⁴ $J_C = J_{C0}(1 - T/T_C)^{5/2}(1 + T/T_C)^{-1/2}$; inset: dependencies of the critical current density at 4.2 K on the magnetic field. (d) The critical current densities J_C of various industrial superconducting wires and the YH₆ (shaded area) at 4.2 K. The lower bound of the critical current density of YH₆ was calculated assuming the maximum possible cross section of the sample of $10 \times 50 \mu\text{m}^2$.

It is interesting to compare the experimentally obtained T_C with theoretical calculations based on the Bardeen–Cooper–Schrieffer^{25–27} and the Migdal–Eliashberg^{30,31} theories. In early theoretical works, estimated T_C varies from 250 to 285 K,^{1,13} which is quite far from the experimental values (224–226 K). Considering that the studied pressure range of 165–180 GPa has not been covered in previous papers, we carried out a series of calculations of the superconducting properties of $Im\bar{3}m$ -YH₆ at a fixed pressure of 165 GPa (Supplementary Tables S7–S9) within a semiphenomenological Migdal–Eliashberg^{30,31} approach, where the electron–electron Coulomb repulsion is accounted by one empirical parameter, the Coulomb pseudopotential μ^* , and a parameter-free superconducting density functional theory (SCDFT)^{32,33}.

Numerical solution of the isotropic Migdal–Eliashberg equations³¹ within the standard range of μ^* (cut-off frequency is 6 Ry) = 0.15–0.1 yields a $T_C = 261$ –272 K, which is substantially higher than the experimental value for YH₆. This significant theoretical overestimation of the critical temperature calculated within the harmonic approach motivated us to include the effects of anharmonicity by performing calculations of the phonon band structure and Eliashberg function $\alpha^2F(\omega)$ using the stochastic self-

consistent harmonic approximation (SSCHA)^{34–36} (Supplementary Fig. S21 and S15), which is a non-perturbative variational method to consider anharmonic effects.

At a pressure of 165 GPa, the calculations with the anharmonic $\alpha^2F(\omega)$ show a decrease in the EPC coefficient of YH₆ from 2.24 to 1.71 and an increase of ω_{\log} from 929 to 1333 K due to hardening of the optical phonon modes. The overall influence of anharmonicity on the critical temperature is a decrease by 25 K, and resulting T_C is 236–247 K, which is still higher than the experimental values. To match the experimental data, including isotope coefficient $\alpha_{\text{exp}} = 0.4$, unusually high values of the Coulomb pseudopotential $\mu^*(6 \text{ Ry}) = 0.19\text{--}0.22$ are necessary. Estimations for YH₆ on the basis of DFT-calculated $N(E_F)$, λ , and ω_{\log} give an expected upper critical magnetic field $\mu_0H_{C2}(0) \sim 60 \text{ T}$, a superconducting gap of 48 meV, a coherence length $\xi_{\text{BCS}} = 0.5\sqrt{\hbar/\pi e H_{C2}} = 23 \text{ \AA}$, and $N(E_F)(1 + \lambda) = 1.92$ (Supplementary Table S7).

The experimentally found upper critical magnetic field $\mu_0H_{C2}(0)$ exceeds 110 T (and can reach 158 T in the WHH model), which is more than 2–2.5 times higher than the value predicted within the BCS theory. In other words, the term $N(E_F)(1 + \lambda)$, related to the Sommerfeld constant, is at least 4 times higher than follows from DFT calculations, and ξ_{exp} is 14–17 Å. In this regard, it is curious that possible deviation from the BCS theory of superconductivity in YH₆ was recently noted in Ref. ³⁷ on the basis of the T_C - T_F Uemura plot ³⁸ for superhydrides. A similar disagreement, but less pronounced, is also observed for $Fm\bar{3}m$ -LaH₁₀,² where the experimental $\mu_0H_{C2}(0)$ exceeds the predicted one by ~30–40%.

The SCDFT calculations, which incorporate the phonon-mediated pairing, mass renormalization and pair-breaking Coulomb repulsion under the retardation effect without empirical parameters, such as μ^* in the Migdal-Eliashberg equations, reveal another anomaly of YH₆. Solving the SCDFT gap equation with the anharmonic $\alpha^2F(\omega)$ (Supplementary Information equation (S1)) at 165 GPa yields $T_C = 160 \text{ K}$ and Coulomb potential $\mu = 0.187$, with an error bar of ~2.5% originating from the random sampling step in solving the equation.^{33,39} This value is about 100 K lower than the one found using the Migdal-Eliashberg calculations and 64 K (~28%) below the experimental value (224 K). A similar discrepancy has been reported in LaH₁₀⁴⁰ and within ab initio Eliashberg theory ⁴¹, but in those cases the difference was ~20–30 K. Apart from this, the 64 K underestimation still indicates anomalously large impact of the Coulomb repulsion and implies something beyond the conventional phonon-mediated superconductivity that boosts the critical temperature up to the experimentally observed value.

Within the conventional mechanism, we can try to explain the discrepancy using at least two hypotheses. First, it could be achieved in the fully anisotropic Eliashberg equation.^{42,43} In the work of Heil et al.,¹³ at low temperatures the gap function showed a dispersion of width of approximately 30 meV, indicating that the pairing strength depends significantly on the band index and wavenumber. As seen in multiband superconductor MgB₂, averaging approaches using $\alpha^2F(\omega)$ generally yields smaller T_C 's for systems with such band and wavenumber dependences.⁴⁴ Although the SCDFT gap equation presumably incorporates the effects included in the Eliashberg equations, they both can give a little different T_C values, as has been pointed out for LaH₁₀.⁴³ Also, large phonon energy scales in the hydride could make relevant the higher order electron-phonon coupling effects beyond the Born-Oppenheimer and the Migdal approximations. Sano et al.⁴⁵ demonstrated that in superconducting sulfur hydride H₃S, the Debye-Waller correction⁴⁶ to the electronic band structure (including the finite spread of the ionic sites) and the vertex correction (including the higher order perturbation of the self-energy due to the electron-phonon interaction) both change the calculated value of T_C by several tens of Kelvins. It would be interesting to explore such effects in YH₆.

Conclusions

In this research, the novel high- T_C superconductor $Im\bar{3}m$ -YH₆ was discovered together with $I4/mmm$ -YH₄ and YH₇ at pressures of 160–196 GPa, confirming theoretical predictions.¹ The low-symmetry molecular yttrium hydride $P1$ -YH_{7+x} ($x = \pm 0.5$) was found to cause complex XRD patterns at 166 GPa. The measured critical temperature of $Im\bar{3}m$ -YH₆ is 224 K, which is unexpectedly lower than the theoretically predicted value (>273 K).⁹ The observed upper critical magnetic field $\mu_0 H_{C2}(0) = 116$ – 158 T is more than two times larger than the calculated one (~ 60 T). Electrical transport measurements show that the critical current density J_C in our samples may exceed 3500 A/mm² at 0 K, which opens remarkable prospects for YH₆ in superconducting electronics.

Anharmonic effects in $Im\bar{3}m$ -YH₆ lead to a decrease in the EPC coefficient from 2.24 to 1.71 and lowering the critical temperature by 25 K. An anomalously large impact of the Coulomb repulsion was found in yttrium hexahydride within both the Migdal–Eliashberg and the SCDFT approaches. The calculated T_C agreed with the experimental critical temperature and the isotope coefficient only when the Coulomb pseudopotential $\mu^*(6 \text{ Ry})$ was equal to 0.19–0.22 and anharmonicity is included in the calculations. The parameter-free SCDFT calculations for YH₆ give substantially lower $T_C = 160$ K which implies importance of effects missing in the conventional Migdal–Eliashberg theory.

Author Contributions

& These authors contributed equally to this work.

D.V.S., I.A.T., A.G.I., A.G.G., V.B.P., E.G., V.V.S. performed the experiment. I.A.T. deposited electrodes and performed the superconductivity measurements. A.V.S., O.A.S., V.M.P. performed the magnetotransport experiments in high magnetic fields and participated in data processing and discussions. A.G.K. and A.R.O. prepared the theoretical analysis. A.B., I.E., R.B., M.C., F.M., L.M. calculated the anharmonic phonon density of states and Eliashberg function. R.A. performed the calculations of T_C within the SCDFT formalism. D.V.S., A.G.K., A.R.O. wrote the manuscript. All authors provided critical feedback and helped shape the research, analysis, and manuscript.

Acknowledgements

The work on the high-pressure experiments was supported by the Ministry of Science and Higher Education of the Russian Federation within the state assignment of the FSRC “Crystallography and Photonics” of RAS and by the Russian Science Foundation (Project No. 19-12-00414). A.G.K. thanks the Russian Foundation for Basic Research (project № 19-03-00100) and the Foundation for Assistance to Small Innovative Enterprises (grant UMNiK № 13408GU/2018) for the financial support of this work. A.R.O., D.V.S. and A.G.K. thank the Russian Science Foundation (grant 19-72-30043). The authors express their gratitude to the staff of the BL10XU (High Pressure Research) station of SPring-8 synchrotron research facilities, especially to Saori Kawaguchi (JASRI) for the tremendous assistance in the use of the station’s equipment before and after the experiment. Portions of this work were performed at GeoSoilEnviroCARS (The University of Chicago, Sector 13), Advanced Photon Source (APS), Argonne National Laboratory. GeoSoilEnviroCARS is supported by the National Science Foundation — Earth Sciences (EAR — 1634415) and Department of Energy — GeoSciences (DE-FG02-94ER14466). Use of the GSECARS Raman Lab System was supported by the NSF MRI Proposal (EAR-1531583). This research used the resources of the Advanced Photon Source, a U.S. Department of Energy (DOE) Office of Science User Facility operated for the DOE Office of Science by Argonne National Laboratory under contract No. DE-AC02-06CH11357. I.E.

and R.B. acknowledge support from the European Research Council (ERC) under the European Union's Horizon 2020 research and innovation programme (grant agreement no. 802533).

References

1. Liu, H., Naumov, I. I., Hoffmann, R., Ashcroft, N. W. & Hemley, R. J. Potential high-Tc superconducting lanthanum and yttrium hydrides at high pressure. *PNAS* **114**, 6990–6995 (2017).
2. Drozdov, A. P. *et al.* Superconductivity at 250 K in lanthanum hydride under high pressures. *Nature* **569**, 528 (2019).
3. Somayazulu, M. *et al.* Evidence for Superconductivity above 260 K in Lanthanum Superhydride at Megabar Pressures. *Phys. Rev. Lett.* **122**, 027001 (2019).
4. Struzhkin, V. *et al.* Superconductivity in La and Y hydrides: Remaining questions to experiment and theory. *Matter and Radiation at Extremes* **5**, 028201 (2020).
5. APS -APS March Meeting 2020 - Event - Superconductivity in Yttrium and Thorium Polyhydrides: a Route to Industrial Applications. in *Bulletin of the American Physical Society* vol. Volume 65, Number 1 (American Physical Society).
6. Semenok, D. V. *et al.* Superconductivity at 161 K in thorium hydride ThH10: Synthesis and properties. *Mat. Today* **33**, 36–44 (2020).
7. Kruglov, I. A. *et al.* Uranium polyhydrides at moderate pressures: prediction, synthesis, and expected superconductivity. *Sci. Adv.* **4**, eaat9776 (2018).
8. Salke, N. P. *et al.* Synthesis of clathrate cerium superhydride CeH₉ at 80 GPa with anomalously short H-H distance. *arXiv:1805.02060* <https://arxiv.org/ftp/arxiv/papers/1805/1805.02060.pdf> (2018).
9. Zhou, D. *et al.* Superconducting praseodymium superhydrides. *Science Advances* **6**, eaax6849 (2020).
10. Zhou, D. *et al.* High-Pressure Synthesis of Magnetic Neodymium Polyhydrides. *J. Am. Chem. Soc.* **142**, 2803–2811 (2020).
11. Li, Y. *et al.* Pressure-stabilized superconductive yttrium hydrides. *Scientific Reports* **5**, 09948 (2015).
12. Grishakov, K. S., Degtyarenko, N. N. & Mazur, E. A. Electron, Phonon, and Superconducting Properties of Yttrium and Sulfur Hydrides under High Pressures. *J. Exp. Theor. Phys.* **128**, 105–114 (2019).
13. Heil, C., di Cataldo, S., Bachelet, G. B. & Boeri, L. Superconductivity in sodalite-like yttrium hydride clathrates. *Phys. Rev. B* **99**, 220502 (2019).
14. Oganov, A. R. & Glass, C. W. Crystal structure prediction using ab initio evolutionary techniques: Principles and applications. *J. Chem. Phys.* **124**, 244704 (2006).
15. Oganov, A. R., Lyakhov, A. O. & Valle, M. How Evolutionary Crystal Structure Prediction Works—and Why. *Acc. Chem. Res.* **44**, 227–237 (2011).
16. Lyakhov, A. O., Oganov, A. R., Stokes, H. T. & Zhu, Q. New developments in evolutionary structure prediction algorithm USPEX. *Computer Physics Communications* **184**, 1172–1182 (2013).
17. Oganov, A. R., Ma, Y., Lyakhov, A. O., Valle, M. & Gatti, C. Evolutionary crystal structure prediction as a method for the discovery of minerals and materials. *Rev. Mineral Geochem* 271–298 (2010).
18. Kong, P. P. *et al.* Superconductivity up to 243 K in yttrium hydrides under high pressure. *arXiv:1909.10482 [cond-mat]* (2019).
19. APS -APS March Meeting 2020 - Event - Superconductivity at 262 K in Yttrium Superhydride at High Pressures. in *Bulletin of the American Physical Society* (American Physical Society).
20. Werthamer, N. R., Helfand, E. & Hohenberg, P. C. Temperature and Purity Dependence of the Superconducting Critical Field, H_{c2} . III. Electron Spin and Spin-Orbit Effects. *Phys. Rev.* **147**, 295–302 (1966).

21. Ginzburg, V. L. & Landau, L. D. On the Theory of superconductivity. *Zh.Eksp.Teor.Fiz.* **20**, 1064–1082 (1950).
22. Baumgartner, T. *et al.* Effects of neutron irradiation on pinning force scaling in state-of-the-art Nb₃Sn wires. *Supercond. Sci. Technol.* **27**, 015005 (2013).
23. Carbotte, J. P. Properties of boson-exchange superconductors. *Rev. Mod. Phys.* **62**, 1027–1157 (1990).
24. Dew-Hughes, D. Flux pinning mechanisms in type II superconductors. *The Philosophical Magazine: A Journal of Theoretical Experimental and Applied Physics* **30**, 293–305 (1974).
25. Griessen, R. *et al.* Evidence for mean free path fluctuation induced pinning in YBa₂Cu₃O₇ and YBa₂Cu₄O₈ films. *Phys. Rev. Lett.* **72**, 1910–1913 (1994).
26. Schwartz, J. *et al.* Status of high temperature superconductor based magnets and the conductors they depend upon. *arXiv:1108.1634 [physics]* (2011).
27. Cooper, L. N. Bound Electron Pairs in a Degenerate Fermi Gas. *Phys. Rev.* **104**, 1189–1190 (1956).
28. Bardeen, J., Cooper, L. N. & Schrieffer, J. R. Microscopic Theory of Superconductivity. *Phys. Rev.* **106**, 162–164 (1957).
29. Bardeen, J., Cooper, L. N. & Schrieffer, J. R. Theory of Superconductivity. *Phys. Rev.* **108**, 1175–1204 (1957).
30. Migdal, A. B. Interaction between electrons and lattice vibrations in a normal metal. *JETP* **34**, 996–1001 (1958).
31. Eliashberg, G. M. Interactions between Electrons and Lattice Vibrations in a Superconductor. *JETP* **11**, 696–702 (1959).
32. Lüders, M. *et al.* Ab initio theory of superconductivity. I. Density functional formalism and approximate functionals. *Phys. Rev. B* **72**, 024545 (2005).
33. Marques, M. A. L. *et al.* Ab initio theory of superconductivity. II. Application to elemental metals. *Phys. Rev. B* **72**, 024546 (2005).
34. Errea, I., Calandra, M. & Mauri, F. Anharmonic free energies and phonon dispersions from the stochastic self-consistent harmonic approximation: Application to platinum and palladium hydrides. *Phys. Rev. B* **89**, 064302 (2014).
35. Bianco, R., Errea, I., Paulatto, L., Calandra, M. & Mauri, F. Second-order structural phase transitions, free energy curvature, and temperature-dependent anharmonic phonons in the self-consistent harmonic approximation: Theory and stochastic implementation. *Phys. Rev. B* **96**, 014111 (2017).
36. Monacelli, L., Errea, I., Calandra, M. & Mauri, F. Pressure and stress tensor of complex anharmonic crystals within the stochastic self-consistent harmonic approximation. *Phys. Rev. B* **98**, 024106 (2018).
37. Talantsev, E. F. Characterization of near-room-temperature superconductivity in yttrium superhydrides. *arXiv:1912.10941 [cond-mat]* (2019).
38. Uemura, Y. J. Dynamic superconductivity responses in photoexcited optical conductivity and Nernst effect. *Phys. Rev. Materials* **3**, 104801 (2019).
39. Akashi, R., Nakamura, K., Arita, R. & Imada, M. High-temperature superconductivity in layered nitrides beta-LixMNCI (M = Ti, Zr, Hf): Insights from density functional theory for superconductors. *Phys. Rev. B* **86**, 054513 (2012).
40. Kruglov, I. A. *et al.* Superconductivity of LaH₁₀ and LaH₁₆ polyhydrides. *Phys. Rev. B.* **101**, 024508 (2020).
41. Sanna, A. *et al.* Ab initio Eliashberg Theory: Making Genuine Predictions of Superconducting Features. *J. Phys. Soc. Jpn.* **87**, 041012 (2018).
42. Margine, E. R. & Giustino, F. Anisotropic Migdal-Eliashberg theory using Wannier functions. *Phys. Rev. B* **87**, 024505 (2013).

43. Errea, I. *et al.* Quantum crystal structure in the 250-kelvin superconducting lanthanum hydride. *Nature* **578**, 66–69 (2020).
44. Choi, H. J., Roundy, D., Sun, H., Cohen, M. L. & Louie, S. G. First-principles calculation of the superconducting transition in MgB₂ within the anisotropic Eliashberg formalism. *Phys. Rev. B* **66**, 020513 (2002).
45. Sano, W., Koretsune, T., Tadano, T., Akashi, R. & Arita, R. Effect of Van Hove singularities on high-T_c superconductivity in H₃S. *Phys. Rev. B* **93**, 094525 (2016).
46. Yussouff, M., Rao, B. K. & Jena, P. Reverse isotope effect on the superconductivity of PdH, PdD, and PdT. *Solid State Communications* **94**, 549–553 (1995).
47. Kvashnin, A. G., Semenov, D. V., Kruglov, I. A., Wrona, I. A. & Oganov, A. R. High-Temperature Superconductivity in Th-H System at Pressure Conditions. *ACS Applied Materials & Interfaces* **10**, 43809–43816 (2018).

SUPPLEMENTARY INFORMATION

Anomalous high-temperature superconductivity in YH_6

Ivan A. Troyan,^{1,&} Dmitrii V. Semenok,^{2,&,*} Alexander G. Kvashnin,^{2,&,*} Andrey V. Sadakov,³
Oleg A. Sobolevskiy,³ Vladimir M. Pudalov,³ Anna G. Ivanova,¹ Vitali B. Prakapenka,⁴ Eran Greenberg,⁴
Alexander G. Gavriluk,^{1,5} Viktor V. Struzhkin,⁶ Aitor Bergara,^{10,11,12} Ion Errea,^{11,12,13} Raffaello Bianco,¹¹
Matteo Calandra,^{14,15,16} Francesco Mauri,^{16,17} Lorenzo Monacelli,^{16,17} Ryosuke Akashi,¹⁸
and Artem R. Oganov^{2,8,9,*}

¹ Shubnikov Institute of Crystallography, Federal Scientific Research Center Crystallography and Photonics, Russian Academy of Sciences, Moscow 119333, 59 Leninskii Prospekt, Russia

² Skolkovo Institute of Science and Technology, Skolkovo Innovation Center, 3 Nobel Street, Moscow 121205, Russia

³ P. N. Lebedev Physical Institute, Russian Academy of Sciences, Moscow 119991, Russia

⁴ Center for Advanced Radiation Sources, The University of Chicago, 5640 South Ellis Avenue, Chicago, Illinois 60637, USA

⁵ IC RAS Institute for Nuclear Research, Russian Academy of Sciences, Moscow, 117312 Russia

⁶ Center for High Pressure Science and Technology Advanced Research, Shanghai 201203, China

⁸ Moscow Institute of Physics and Technology, 9 Institutsky Lane, Dolgoprudny 141700, Russia

⁹ International Center for Materials Discovery, Northwestern Polytechnical University, Xi'an 710072, China

¹⁰ Departamento de Física de la Materia Condensada, University of the Basque Country (UPV/EHU), 48080 Bilbao, Basque Country, Spain

¹¹ Centro de Física de Materiales CFM, CSIC-UPV/EHU, Paseo Manuel de Lardizabal 5, 20018 Donostia, Basque Country, Spain

¹² Donostia International Physics Center (DIPC), Manuel Lardizabal pasealekua 4, 20018 Donostia, Basque Country, Spain

¹³ Fisika Aplikatua 1 Saila, University of the Basque Country (UPV/EHU), Europa Plaza 1, 20018 Donostia, Basque Country, Spain

¹⁴ Dipartimento di Fisica, Università di Trento, Via Sommarive 14, 38123 Povo, Italy

¹⁵ Sorbonne Université, CNRS, Institut des Nanosciences de Paris, UMR7588, F-75252 Paris, France

¹⁶ Graphene Labs, Fondazione Istituto Italiano di Tecnologia, Via Morego, I-16163 Genova, Italy

¹⁷ Dipartimento di Fisica, Università di Roma Sapienza, Piazzale Aldo Moro 5, I-00185 Roma, Italy

¹⁸ University of Tokyo, 7-3-1 Hongo, Bunkyo, Tokyo 113-8654, Japan

Table of contents

Methods	2
Experiment	2
Theory	3
Crystal structures	5
Thermodynamic stability of Y–H compounds	6
X-ray diffraction data	9
Raman spectra	10
Critical parameters of superconducting state of YH_6	11
Eliashberg functions of yttrium hydrides	13
Equations for calculating T_C and related parameters	15
Electronic and phonon properties of yttrium hydrides	17
Elastic properties of Y–H phases.....	20
References	22

Methods

Experiment

To perform this experimental study, three diamond anvil cells (DACs) — K1, M1, and M3 — were loaded. The diameter of the working surface of the diamond anvils was 280 μm bevelled at an angle of 8.5° to a culet of 50 μm . The X-ray diffraction (XRD) patterns of all samples in the DACs were recorded at the GSECARS synchrotron beamline at the Advanced Photon Source (APS), Argonne, U.S. An X-ray beam with an energy of 42 and 37 keV and wavelength $\lambda = 0.295$ and 0.334 \AA was focused to $2.5 \times 3.5 \mu\text{m}$. A Pilatus 1M CdTe detector was placed at a distance of ~ 200 mm from the sample. The exposure time was 20–60 s. LaB₆ standard was used for the detector geometry calibration. The XRD data were analysed and integrated using Dioptas software package (version 0.4).¹ The full profile analysis of the diffraction patterns and the calculation of the unit cell parameters were performed in JANA2006 computing system² using the Le Bail method.³

The heating of the sample was performed at GSECARS by $\sim 10^5$ pulses of a Nd:YAG infrared laser with a wavelength $\lambda = 1.064 \mu\text{m}$, the duration of each pulse was 1 μs .⁴ The temperature measurements were carried out using the gray body radiation fit within the Planck function at the laser heating system of the GSECARS beamline of the APS. The applied pressure was measured by the edge position of the Raman signal of diamond⁵ using Acton SP2500 spectrometer with PIXIS:100 spectroscopic-format CCD.⁶ The pressure in the DACs was determined by the Raman signal of diamond.⁷

Deuterated ammonium borane (d-AB) was synthesized from NaBD₄ (98 % D, SigmaAldrich) via the reaction with ammonium formate HCOONH₄ in tetrahydrofuran followed by isotopic substitution (H \rightarrow D) in D₂O⁸. After removing of solvents and vacuum drying, the obtained ND₃BD₃ was analyzed by ¹H NMR and Raman spectroscopy. Deuterium content in the product was found to be 92 %. Partially substituted NH₃BD₃ and ND₃BH₃ may be synthesized in a similar way for later use as a source of HD.

Magnetotransport measurements were performed on samples with at least two hydride phases and, therefore, the voltage contacts of the Van der Pauw scheme might be connected to low- T_C phase. As a result the superconducting transition in YH₆ can be observed as an upward feature of the R(T,H) curves due to the shunting effect in the fine-grained samples.

For the Dew-Hughes model⁹ of the pinning force $f \sim h^p(1-h)^q$, the parameters should be $p=0.5$, $q=2$, $h_{\text{max}}=0.2$, which is close to the fit of the experimental data (Fig. S13a). Depinning critical current for this type of pinning can be described within the single vortices model, where vortices are pinned on randomly distributed weak pinning centers via spatial fluctuations of the charge carrier mean free path, or in other words "dl-pinning".

Table S1. Experimental parameters of the DACs.

DAC	Pressure, GPa	Gasket	Sample size, μm	Composition/load
K1	166	CaF ₂ /epoxy	10	Y/NH ₃ BH ₃
M1	165	CaF ₂ /epoxy	12	Y/NH ₃ BH ₃
M3	172	CaF ₂ /epoxy	9	Y/NH ₃ BH ₃
D1	172	CaF ₂ /epoxy	15	Y/ND ₃ BD ₃

Theory

The computational predictions of the thermodynamic stability of the Y–H phase at 150, 200, and 250 GPa were carried out using the variable-composition evolutionary algorithm USPEX.^{10–12} The first generation consisting of 120 structures was produced using random symmetric¹² and random topology¹³ generators, whereas all subsequent generations contained 20% of random structures and 80% of those created using heredity, softmutation, and transmutation operators. The evolutionary searches were combined with structure relaxations using the density functional theory (DFT)^{14,15} within the Perdew–Burke–Ernzerhof functional (generalized gradient approximation)¹⁶ and the projector augmented wave method^{17,18} as implemented in the VASP code.^{19–21} The kinetic energy cutoff for plane waves was 600 eV. The Brillouin zone was sampled using the Γ -centred k -points meshes with a resolution of $2\pi \times 0.05 \text{ \AA}^{-1}$. The methodology is similar to those used in our previous works.^{22,23}

The equations of state of the discovered YH₄, YH₆, and YH₇ phases were calculated using the same methods with the plane wave kinetic energy cutoff set to 700 eV. We also calculated the phonon densities of states of the studied materials using the finite displacements method (VASP and PHONOPY).^{24,25}

The calculations of superconducting T_C were carried out using QUANTUM ESPRESSO (QE) package.^{26,27} The phonon frequencies and electron–phonon coupling (EPC) coefficients were computed using the density functional perturbation theory,²⁸ employing the plane-wave pseudopotential method and Perdew–Burke–Ernzerhof exchange–correlation functional.¹⁶ In our ab initio calculations of the electron–phonon coupling (EPC) coefficient λ , the first Brillouin zone was sampled using a $3 \times 3 \times 3$ or $4 \times 4 \times 4$ q -points mesh and a denser $16 \times 16 \times 16$ k -points mesh (with the Gaussian smearing and $\sigma = 0.005$ Ry, which approximates the zero-width limits in the calculation of λ) for YH₇ and YH₄.

The calculations of the Eliashberg function of $Im\bar{3}m$ -YH₆ were performed using $6 \times 6 \times 6$ q -points and $60 \times 60 \times 60$ k -points meshes. T_C was calculated by solving the isotropic Eliashberg equations²⁹ using the iterative self-consistent method for the imaginary part of the order parameter $\Delta(T, \omega)$ (superconducting gap) and the renormalization wave function $Z(T, \omega)$ assuming that the Coulomb repulsion between the electrons can be parametrized with the μ^* . More approximate estimates of T_C were made using the Allen–Dynes formula.³⁰

We also calculated the superconducting transition temperature T_C of YH₆ by solving the gap equation in the density functional theory for superconductors (SCDFT):^{31,32}

$$\Delta_{nk}(T) = -Z_{nk}(T)\Delta_{nk}(T) - \frac{1}{2} \sum K_{nkn'k'}(T) \frac{\tanh \beta \xi_{n'k'}}{\xi_{n'k'}} \Delta_{n'k'}(T). \quad (\text{S1})$$

Solving this equation for different temperatures $\beta = 1/T$, we see that the order parameter $\Delta_{n'k'}$ has a nonzero solution below any threshold temperature, which is identified as T_c . Labels n , n' , k , and k' indicate the Kohn–Sham band and crystal wave number indices, respectively. ξ_{nk} is the energy eigenvalue of state nk from the Fermi level, as calculated using the standard Kohn–Sham equation for the normal state. The kernels of the gap equation $Z_{nk}(T)$ and $K_{nkn'k'}(T)$ represent the electron–phonon and electron–electron Coulomb interaction effects, the formulas for which (a study by Kruglov et al.³³ based on the method described in Refs.^{31,32,34,35}) have been constructed so that the perturbation effects, almost the same as those in the Eliashberg equations with the Migdal approximation,^{29,36–38} are included. The solution of equation S1 requires preprocessing to calculate the dielectric matrix for the screened electron–electron Coulomb interaction within the random phase approximation³⁹ and the electronic density of states (DOS) for the normal state. The detailed conditions for the SCDFT calculation are summarized in Table S2.

Table S2. Detailed conditions for calculating T_c of YH_6 within the SCDFT approach.

Crystal structure setting		(YH_6) ₂ simple cubic
Charge density	k	12×12×12 equal mesh
	Interpolation	1st order Hermite Gaussian ³⁹ with a width of 0.020 Ry
Dielectric matrix ϵ	k for bands crossing E_F	15×15×15 equal mesh
	k for other bands	5×5×5 equal mesh
	Number of unoccupied bands [†]	82
	Interpolation	Tetrahedron with the Rath–Freeman treatment ⁴⁰
	cutoff	12.8 Ry
DOS for phononic kernels	k	19×19×19 equal mesh
	interpolation	Tetrahedron with the Blöchl correction ¹⁷
SCDFT gap function	Number of unoccupied bands [‡]	82
	k for the electronic kernel	5×5×5 equal mesh
	k for the KS energies	19×19×19 equal mesh
	Sampling points for bands crossing E_F	6000
	Sampling points for other bands	200
	Sampling error in T_c , %	~2.5

[†]States up to $E_F + 70$ eV are taken into account. [‡]States up to E_F+70 eV are taken into account.

The anharmonic calculations, including the vibrational contribution to the enthalpy, were performed using the stochastic self-consistent harmonic approximation (SSCHA).⁴¹ The anharmonic force constant matrices of $Im\bar{3}m$ - YH_6 were obtained by calculating the forces in $3\times 3\times 3$ supercells and combined with the DFPT electron–phonon calculations performed in a fine $12\times 12\times 12$ mesh to calculate the anharmonic Eliashberg function $\alpha^2F(\omega)$.

Crystal structures

Table S3. Crystal data of the predicted yttrium hydrides and pure elements at 150 GPa.

Phase	Volume, Å ³ /atom	Lattice parameters	Coordinates			
			atom	x	y	z
<i>Fddd</i> -Y	12.88	$a = 16.867 \text{ \AA}$ $b = 4.564 \text{ \AA}$ $c = 2.677 \text{ \AA}$	Y1	-0.187	0.125	0.125
<i>C2/c</i> -H	1.86	$a = 5.332 \text{ \AA}$ $b = 3.052 \text{ \AA}$ $c = 4.484 \text{ \AA}$ $\beta = 142.25^\circ$	H1	0.261	0.083	0.254
			H2	0.148	0.197	0.271
			H3	0.000	-0.159	0.250
			H4	0.000	-0.403	0.250
<i>Fm</i> $\bar{3}m$ -YH	7.643	$a = 3.939 \text{ \AA}$	Y1	0.500	0.500	0.500
			H1	0.000	0.000	0.000
<i>I4/mmm</i> -YH ₃	4.927	$a = 2.995 \text{ \AA}$ $c = 4.392 \text{ \AA}$	Y1	0.000	0.000	0.000
			H1	0.000	0.500	0.250
			H2	0.000	0.000	0.500
<i>I4/mmm</i> -YH ₄	4.072	$a = 2.799 \text{ \AA}$ $c = 5.278 \text{ \AA}$	Y1	0.000	0.000	0.000
			H1	0.000	0.000	-0.371
			H2	0.000	0.500	0.250
<i>Im</i> $\bar{3}m$ -YH ₆	3.339	$a = 3.602 \text{ \AA}$	Y1	0.000	0.000	0.000
			H1	0.250	0.000	0.500
<i>Imm2</i> -YH ₇	3.261	$a = 3.281 \text{ \AA}$ $b = 3.402 \text{ \AA}$ $c = 4.676 \text{ \AA}$	Y1	0.000	0.000	0.018
			H1	0.000	-0.268	-0.333
			H2	0.203	0.000	0.447
			H3	-0.263	0.000	0.384
			H4	0.000	0.500	0.299
<i>P1</i> -YH ₇	3.261	$a = 3.298 \text{ \AA}$ $b = 3.306 \text{ \AA}$ $c = 5.520 \text{ \AA}$ $\alpha = 90.057^\circ$ $\beta = 91.257^\circ$ $\gamma = 60.138^\circ$	Y1	0.348	0.104	-0.351
			Y2	0.000	-0.224	0.148
			H1	0.301	0.125	0.261
			H2	-0.328	0.440	-0.336
			H3	0.493	-0.212	-0.045
			H4	0.292	-0.370	0.462
			H5	-0.149	0.316	-0.127
			H6	-0.005	-0.228	-0.240
			H7	-0.388	-0.326	0.370
			H8	-0.144	-0.395	0.452
			H9	-0.343	0.446	0.163
			H10	0.069	0.246	-0.038
			H11	0.487	0.264	-0.041
			H12	0.395	-0.402	-0.133
			H13	-0.145	0.092	0.452
			H14	-0.393	0.266	0.369
<i>P6₃/mmc</i> -YH ₉	3.051	$a = 3.405 \text{ \AA}$ $c = 5.772 \text{ \AA}$	Y1	0.333	0.666	0.750
			H1	-0.175	-0.351	-0.061
			H2	0.000	0.000	-0.157
			H3	0.333	0.666	0.250
<i>F</i> $\bar{4}3m$ -YH ₉	2.886	$a = 4.869 \text{ \AA}$	Y1	0.500	0.500	0.500
			H1	0.135	0.135	0.135
			H2	-0.116	-0.116	-0.116
			H3	0.750	0.0.75	0.0.75
<i>Fm</i> $\bar{3}m$ -YH ₁₀	2.726	$a = 4.931 \text{ \AA}$	Y1	0.000	0.000	0.000
			H1	0.378	0.378	0.378
			H2	0.250	0.250	0.250

Thermodynamic stability of Y–H compounds

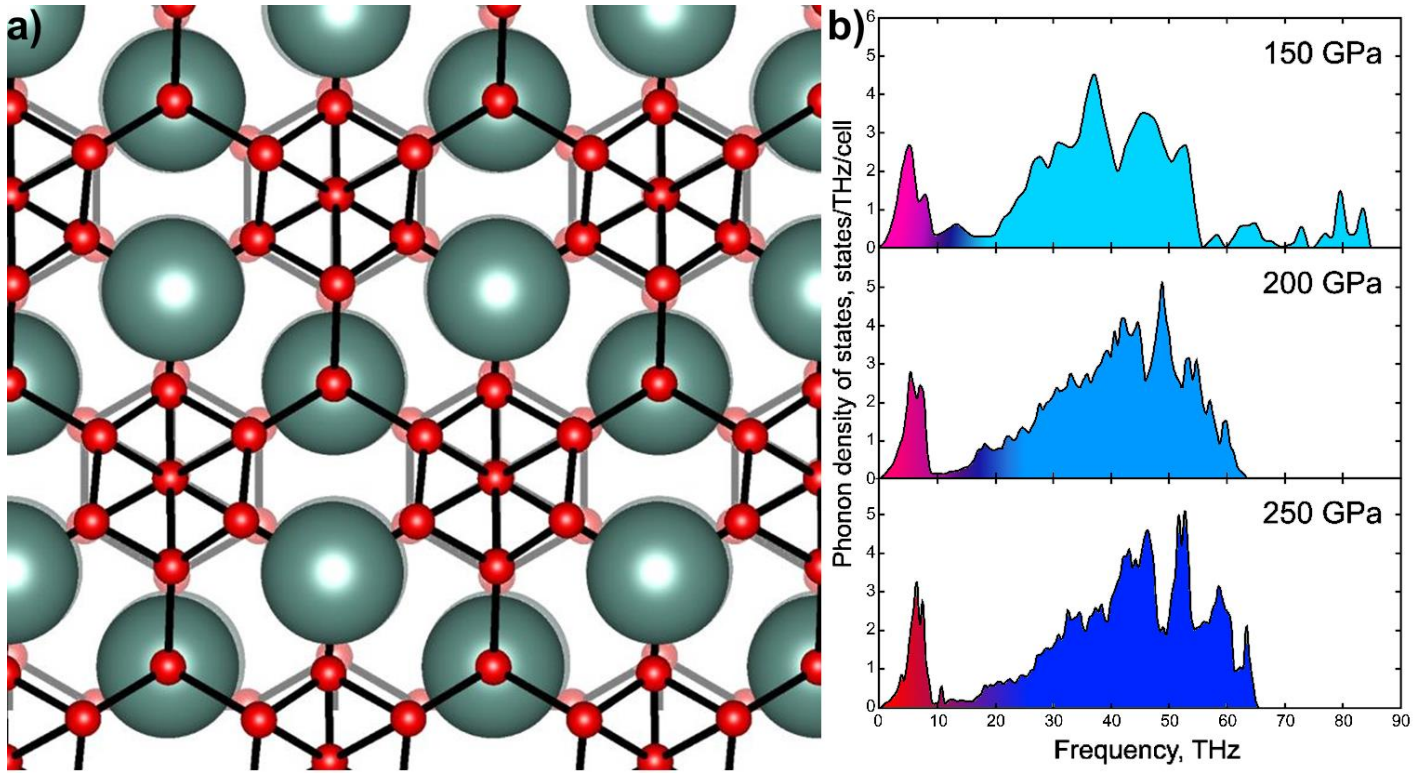


Figure S1. (a) Crystal structure of $P\bar{1}$ -YH₉ (=Y₄H₃₆) with the disordered hydrogen sublattice in comparison with ideal symmetric $P6_3/mmc$ -YH₉ (shaded). The hydrogen atoms are shown in red. (b) Phonon density of states of $P\bar{1}$ -YH₉ at 150, 200, and 250 GPa.

Table S4. Crystal data of predicted pseudohexagonal yttrium hydride $P\bar{1}$ -YH₉ (=Y₄H₃₆) at 200 GPa.

Phase	Volume, Å ³ /atom	Lattice parameters	Coordinates
$P\bar{1}$ -YH ₉	2.662	$a = 3.373 \text{ \AA}$ $b = 5.341 \text{ \AA}$ $c = 3.385 \text{ \AA}$ $\alpha = 89.998^\circ$ $\beta = 119.194^\circ$ $\gamma = 90.129^\circ$	Y1 -0.16542 -0.25018 0.16548
			H1 0.49959 -0.25006 -0.49955
			H2 -0.18944 -0.44497 -0.35591
			H3 -0.18379 -0.05639 -0.35437
			H4 0.35525 -0.05117 -0.35839
			H5 0.34935 -0.05657 0.17690
			H6 -0.16339 0.15138 0.16471
			H7 0.35110 -0.44761 -0.35842
			H8 0.34575 -0.44296 0.17626
			H9 0.16721 -0.34794 -0.16444

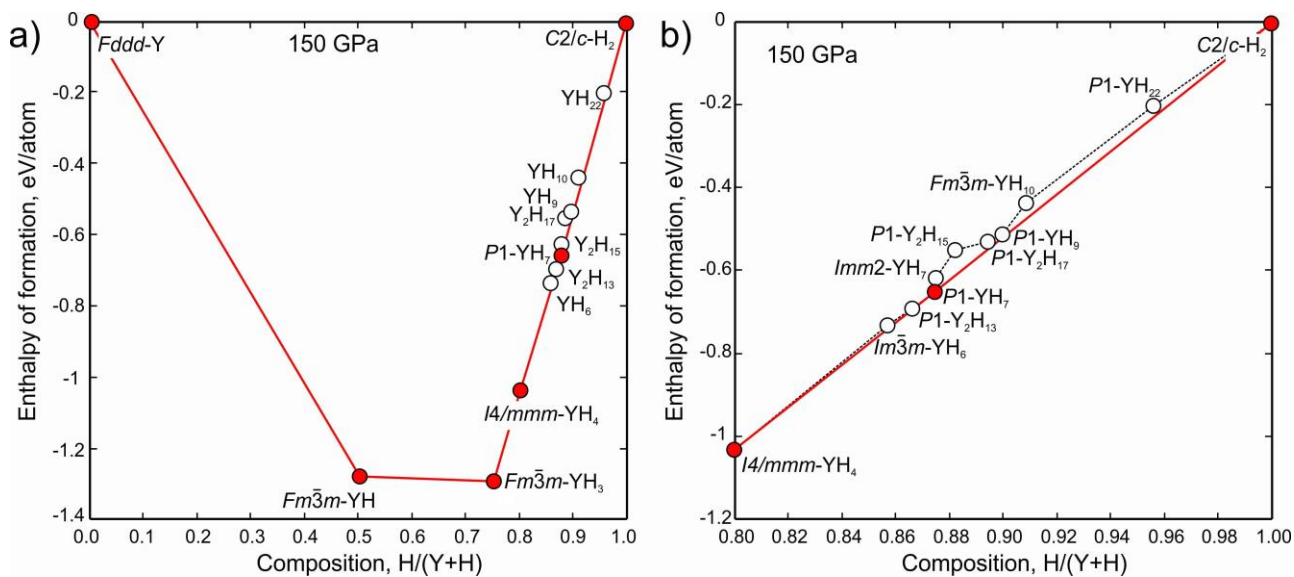


Figure S2. Calculated convex hull of the Y–H system with the zero-point energy (ZPE) at 150 GPa and 0 K: (a) full scale and (b) compositions from 0.8 to 1. Metastable phases are shown by white circles.

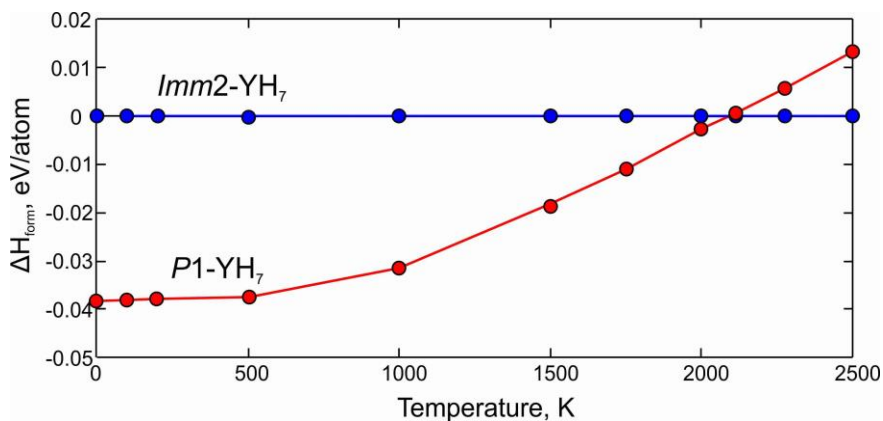


Figure S3. Relative enthalpy of formation of *P1*-YH₇ and *Im $\bar{3}$ m*-YH₇ at 150 GPa.

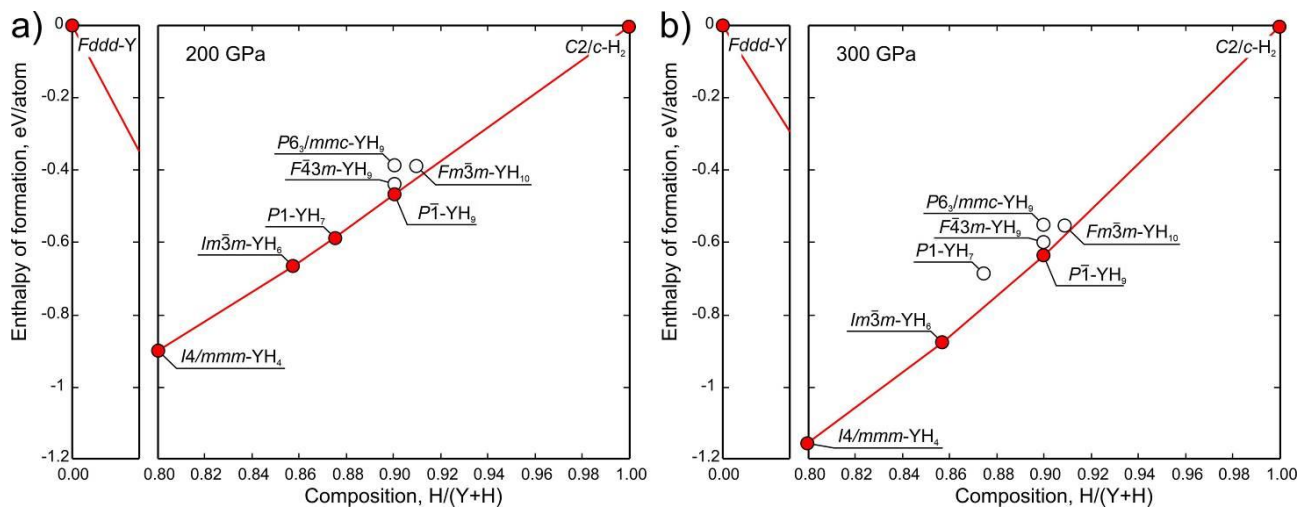


Figure S4. Calculated convex hull of the Y–H system with ZPE at (a) 200 and (b) 300 GPa and 0 K.

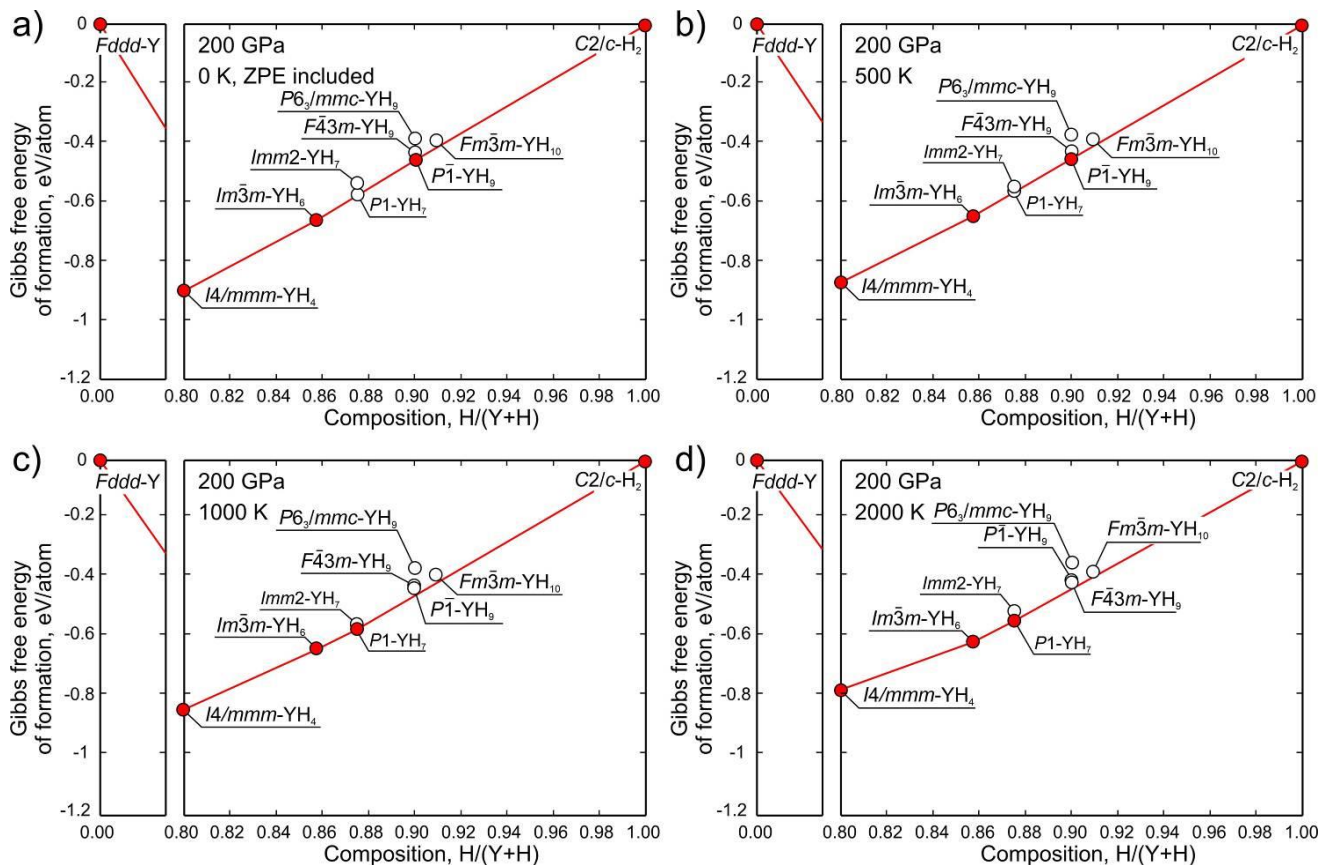


Figure S5. Calculated convex hulls of the Y-H system at 200 GPa and (a) 0 K, (b) 500 K, (c) 1000 K, and (d) 2000 K.

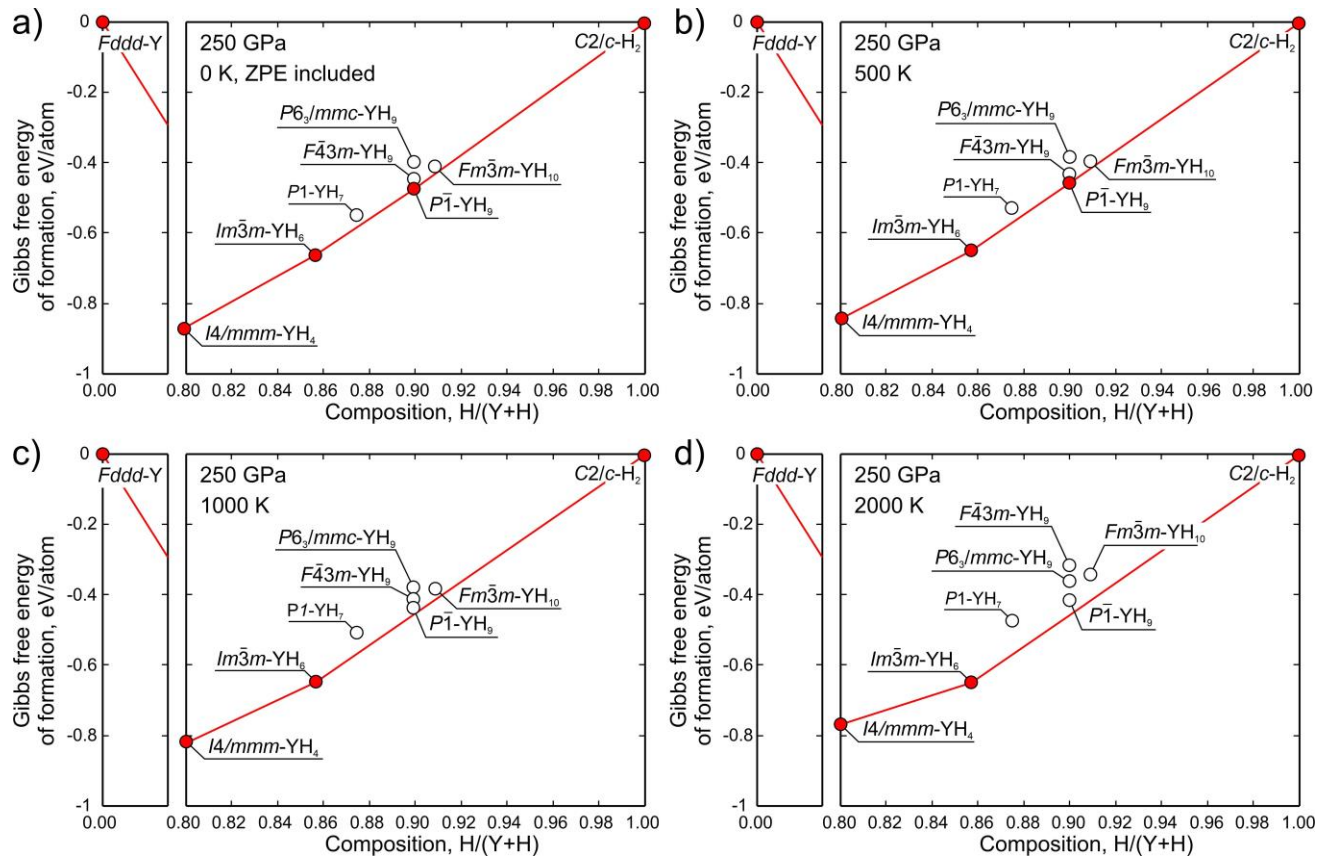


Figure S6. Calculated convex hulls of the Y-H system at 250 GPa and (a) 0 K, (b) 500 K, (c) 1000 K, and (d) 2000 K.

X-ray diffraction data

Table S5. Experimental and predicted lattice parameters and volumes of $I4/mmm$ - YH_4 ($Z = 2$), $Imm2$ - YH_7 ($Z = 2$), and $P1$ - YH_7 ($Z = 2$).

$I4/mmm$ - YH_4									
DAC	Pressure, GPa	a , Å	c , Å	V , Å ³	V_{DFT} , Å ³				
K1	168	2.751(4)	5.15(8)	39.01	40.04				
K3	173	2.68(9)	5.43(3)	39.29	39.70				
K3	180	2.67(6)	5.39(6)	38.65	39.28				
$Imm2$ - YH_7									
DAC	Pressure, GPa	a , Å	b , Å	c , Å	V , Å ³	V_{DFT} , Å ³			
M1	166	3.29(4)	3.33(6)	4.68(7)	51.50	50.85			
$P1$ - YH_7									
DAC	Pressure, GPa	a , Å	b , Å	c , Å	α	β	γ	V , Å ³	V_{DFT} , Å ³
M1	166	3.22(4)	3.27(1)	5.43(8)	93	94.05	61.39	50.22	50.88

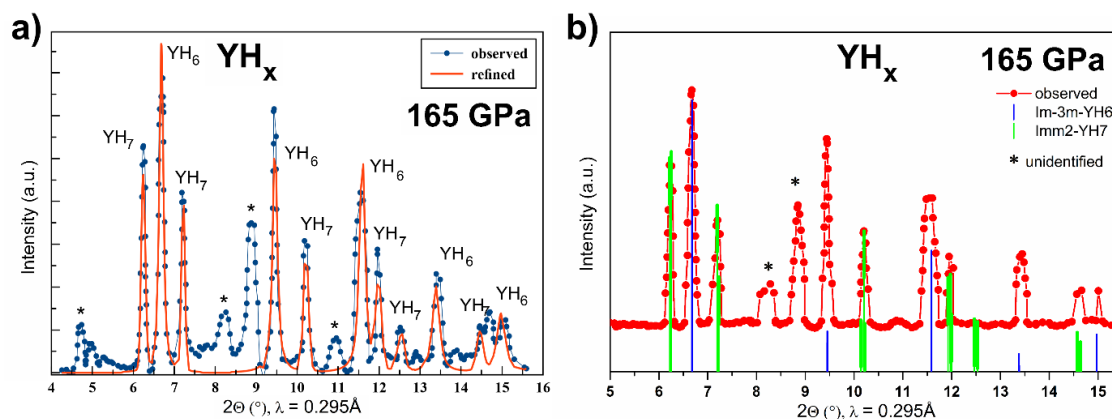


Figure S7. Diffraction patterns (low intensity) of the sample from DAC M1 at 165 GPa: (a) Le Bail refinement by $Im\bar{3}m$ - YH_6 and pseudocubic $Imm2$ - YH_7 ; (b) qualitative interpretation of the smoothed XRD pattern with subtracted background.

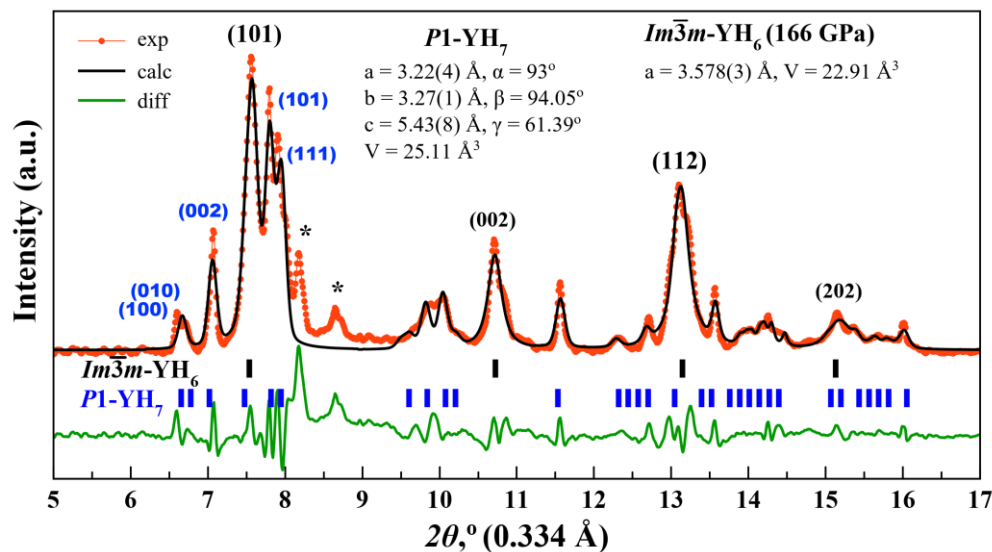


Figure S8. Le Bail refinement of $P1$ - YH_7 and the experimental XRD pattern at 166 GPa (DAC K1). The experimental data, model fit for the structure, and residues are shown in red, black, and green, respectively. Unidentified reflections are marked by asterisks.

Raman spectra

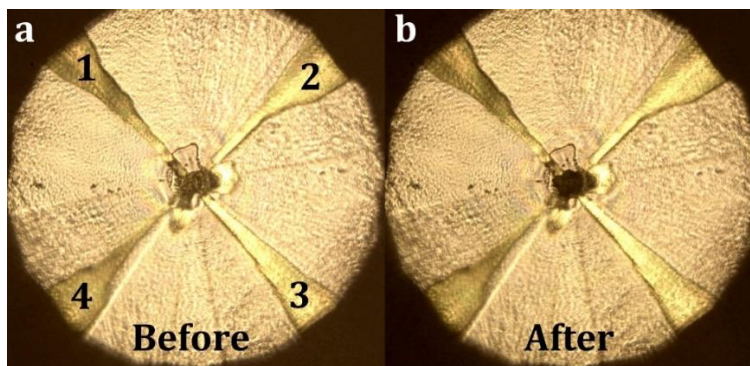


Figure S9. Electrode system of DAC K1 at 166 GPa (a) before and (b) after laser heating. The heating area in the centre of the culet became black.

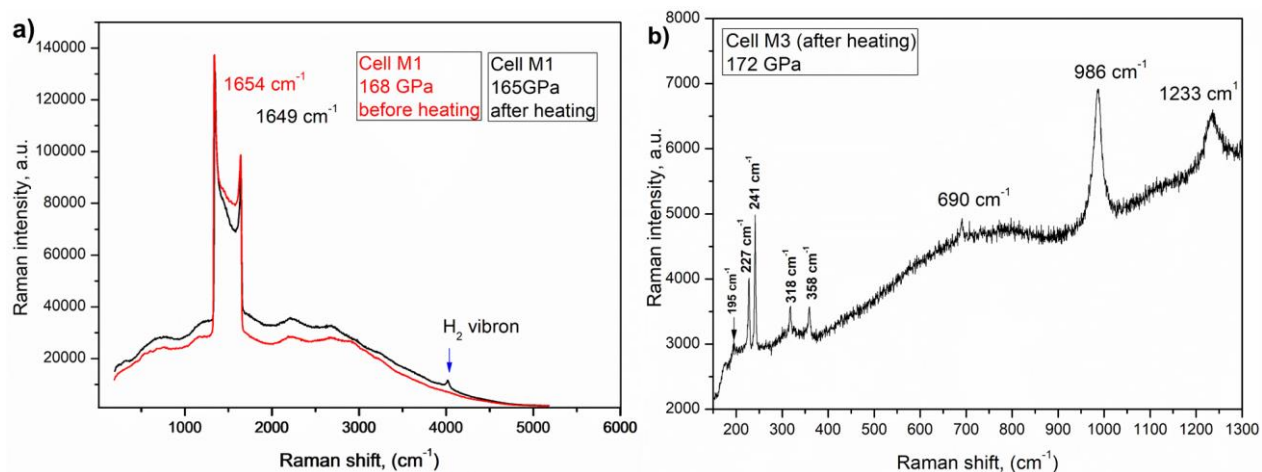


Figure S10. Raman spectra of samples in (a) DAC M1 and (b) DAC M3, before and after heating. Raman signals in DAC M3 may come from impurities of higher molecular yttrium hydrides ($P1\text{-YH}_7\text{-YH}_{7.5}$).

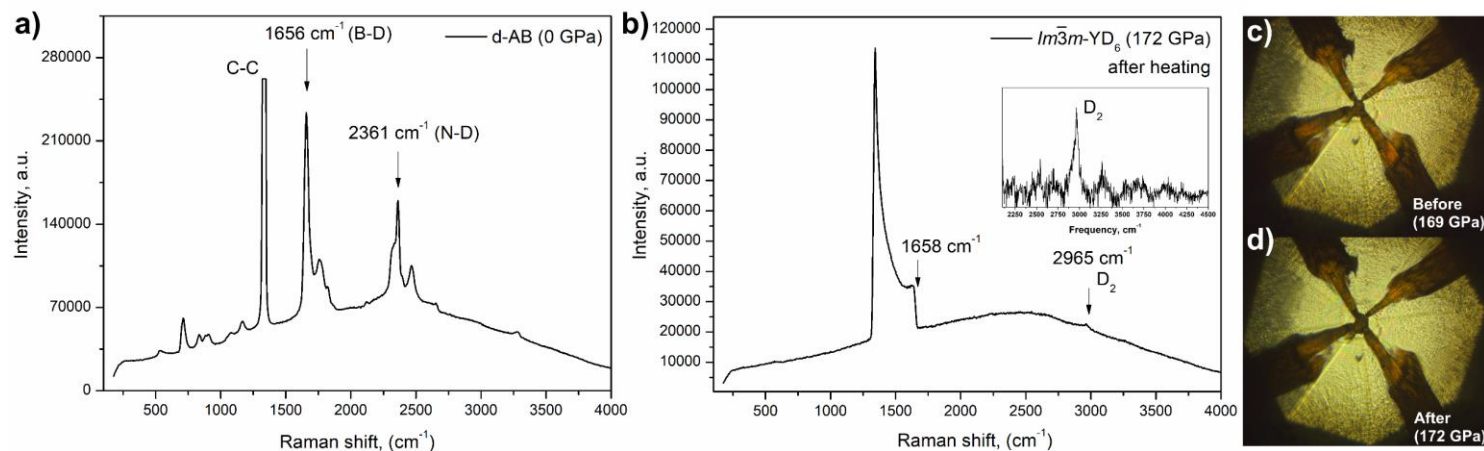


Figure S11. Raman spectra of samples: (a) ND_3BD_3 before the experiment; (b) $\text{Im}\bar{3}m\text{-YD}_6$ after heating (inset: Raman signal of D_2); (c) electrode system of the DAC before and (d) after laser heating.

Critical parameters of superconducting state of YH_6

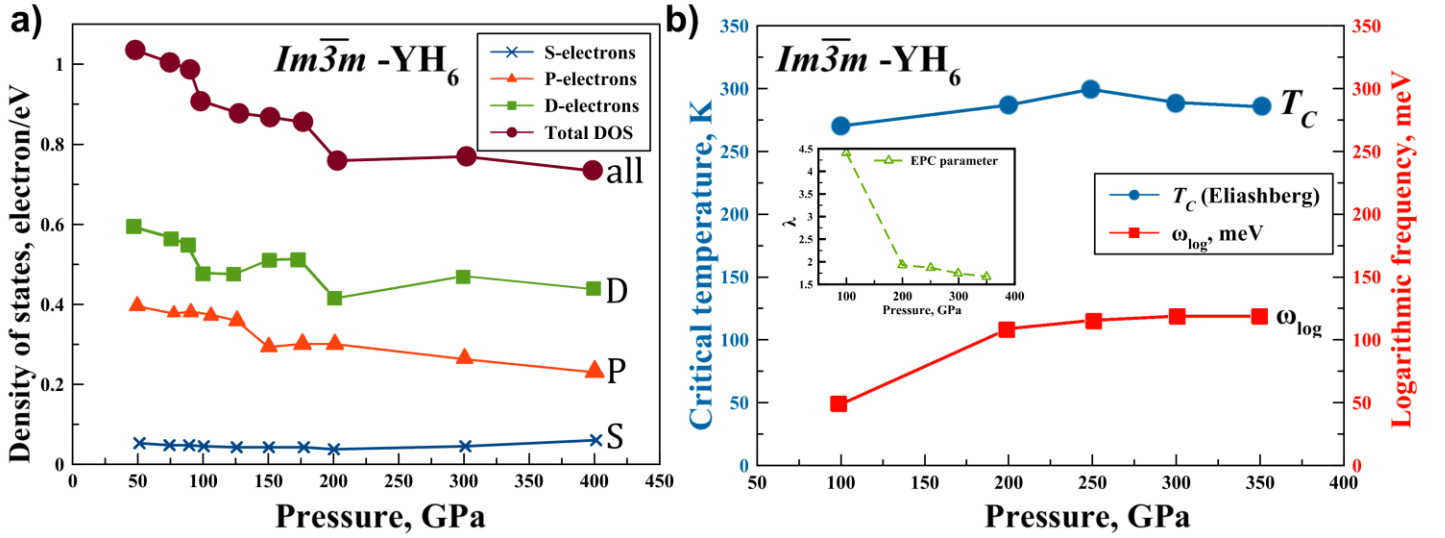


Figure S12. Yttrium hexahydride properties, from previous theoretical studies (see Table S6): (a) contributions of different orbitals to the density of electronic states $N(E_F)$ from Ref. ⁴²; (b) pressure dependence of superconducting parameters T_C , λ , and ω_{\log} from Ref. ⁴³.

Table S6. Calculated superconducting parameters of $\text{Im}\bar{3}m\text{-YH}_6$ from previous theoretical studies.

Parameter	100 GPa	120 GPa	200 GPa	300 GPa
$N(E_F)$, states/eV/f.u.	0.75 ⁴²	0.6 ⁴⁴	0.63 ⁴²	0.69 ⁴³
λ	3.44*	2.93 ⁴⁴	1.93	1.73 ⁴³
ω_{\log} , K	851*	1080, ⁴⁴ 1124 ⁴⁵	1282	1612 ⁴³
T_C , K	233* (A–D)	251–264 ⁴⁴	285 ⁴³	290 ⁴³
Anharmonic ΔT_C , K	-	-34 ⁴⁶	~ 0 ⁴³	~ 0 ⁴³

* Calculated from $\alpha^2F(\omega)$ given in Ref. ⁴³ at $\mu^* = 0.1$.

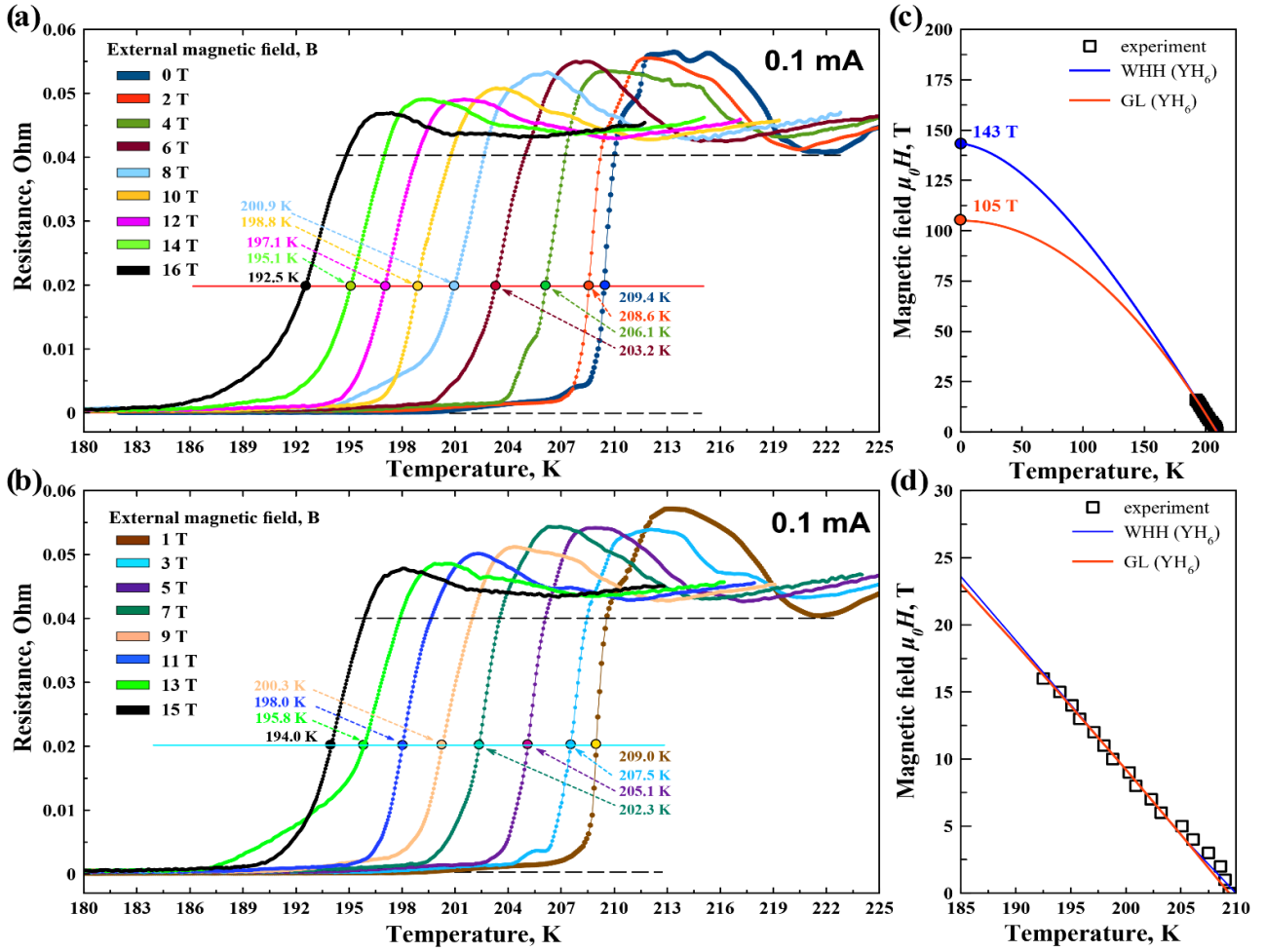


Figure S13. (a, b) Dependence of the electrical resistance (second step) of $Im\bar{3}m$ - YH_6 on the external magnetic field (0–16 T) at 183 GPa: (a) even and (b) odd values of the magnetic field. Critical temperatures were determined at a 50% resistance drop; (c) upper critical magnetic field determined using different theories; (d) dependence of the critical temperature T_C on the applied magnetic field.

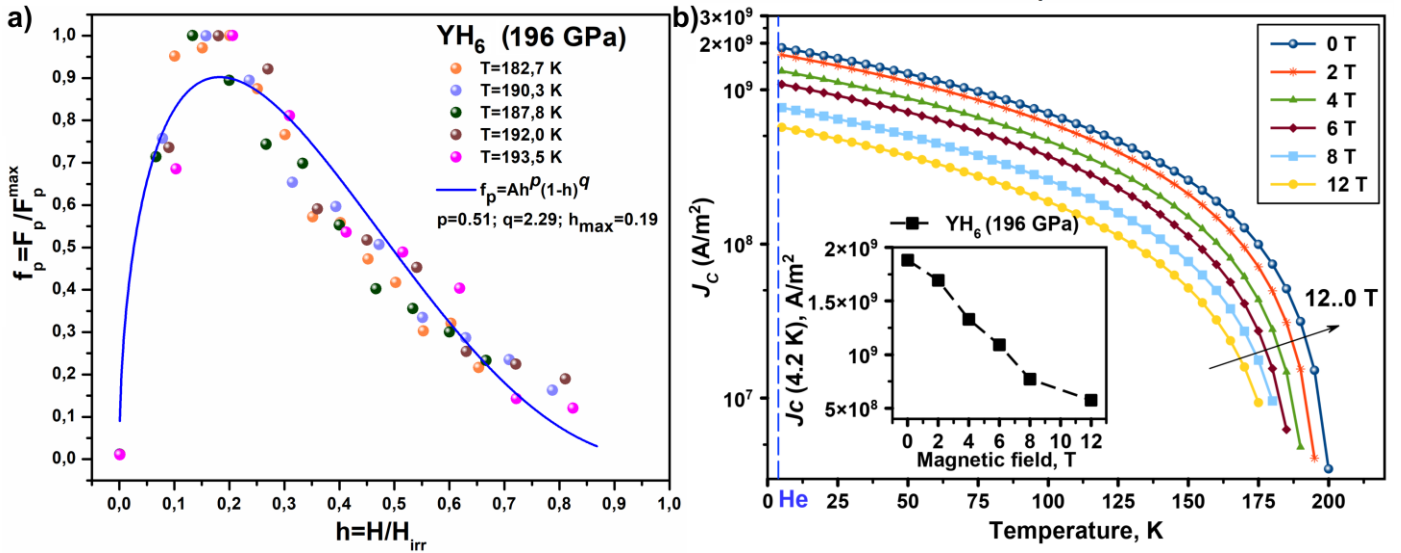


Figure S14. (a) Scaling of the normalized volume pinning forces (F_p/F_p^{\max}) of the YH_6 sample at 196 GPa for several different temperatures versus the reduced field $h = B/B_{\max}$. Experimental data is fitted by the Dew-Hughes⁹ model for surface type normal pinning centers $f \sim h^p(1-h)^q$. (b) Extrapolation of the temperature dependence of the critical current using Landau-Ginzburg model⁴⁷ $J_c = J_{c0}(1 - T/T_c)^{3/2}$; inset: dependencies of the critical current density at 4.2 K on the magnetic field.

Eliashberg functions of yttrium hydrides

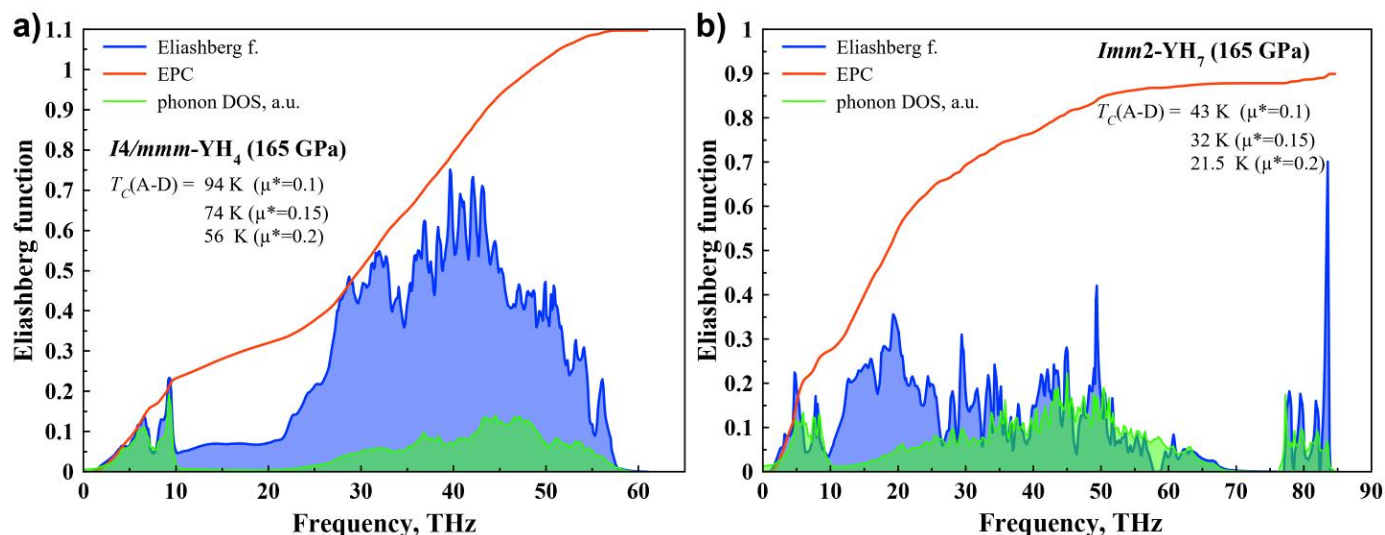


Figure S15. Harmonic Eliashberg functions and superconducting properties calculated in QE with a $16 \times 16 \times 16$ k -grid, $2 \times 2 \times 2$ q -grid, and σ -smearing of 0.01 Ry at 165 GPa for (a) $I4/mmm\text{-YH}_4$ and (b) $Imm2\text{-YH}_7$. “A–D” refers to the Allen–Dynes formula.³⁰

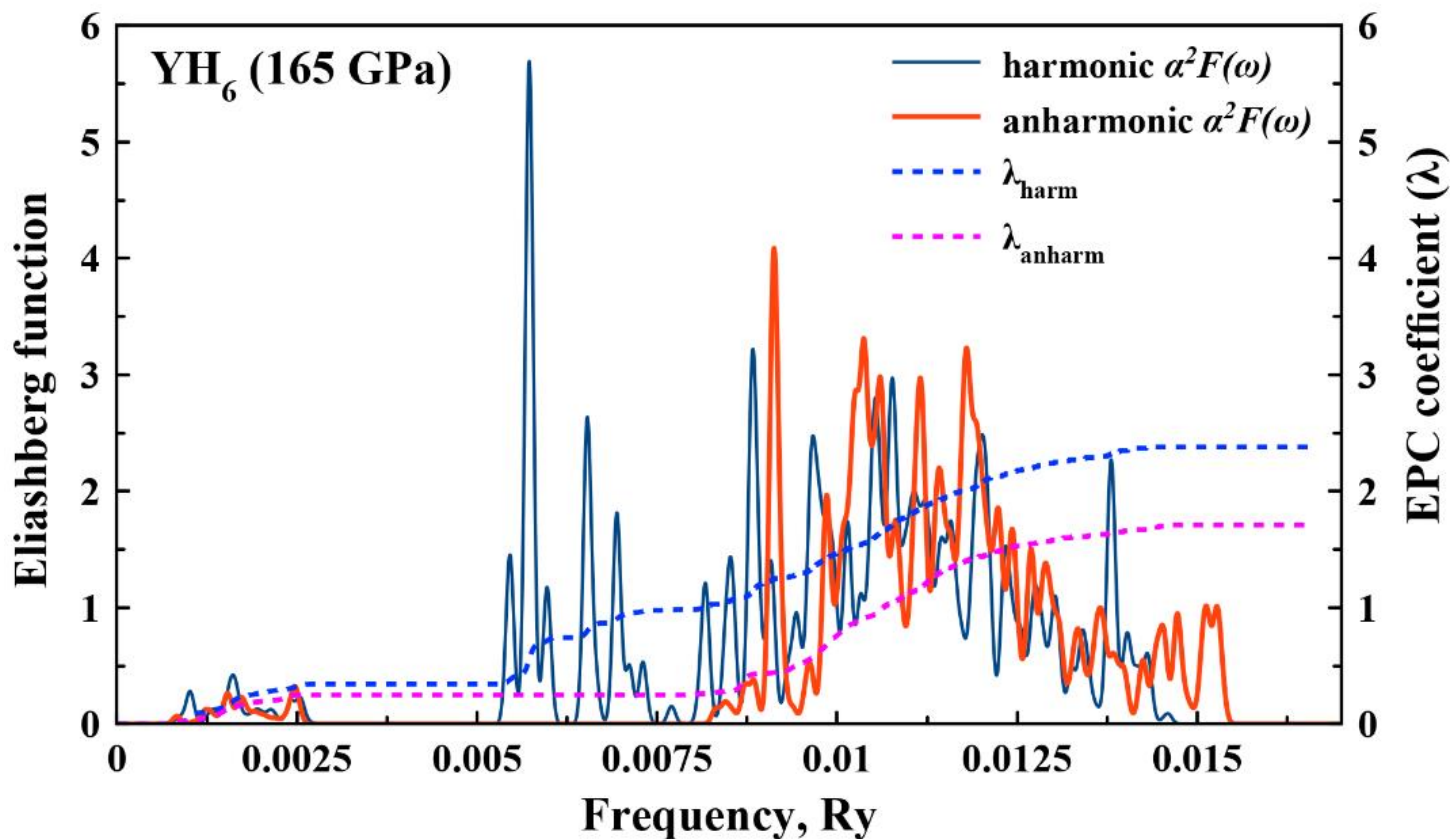


Figure S16. Harmonic and anharmonic Eliashberg functions of $Im\bar{3}m\text{-YH}_6$ at 165 GPa. A $60 \times 60 \times 60$ grid of k -points and $6 \times 6 \times 6$ grid of q -points was used in the calculations.

Table S7. Parameters of the superconducting state of $Im\bar{3}m$ -YH₆, $I4/mmm$ -YH₄, and $Imm2$ -YH₇ at 165 GPa calculated using the isotropic Migdal–Eliashberg equations (E)²⁹ and Allen–Dynes (A–D)³⁰ formula. The Eliashberg functions of YH₄ and YH₇ were calculated using Quantum ESPRESSO package with $4\times 4\times 4$ q -points and $16\times 16\times 16$ k -points grids. Here, γ is the Sommerfeld constant, α is the Allen–Dynes isotopic coefficient.

Parameter	$Im\bar{3}m$ -YH ₆ ^a		$I4/mmm$ -YH ₄	$Imm2$ -YH ₇
	$\mu^* = 0.15-0.1$	$\mu^* = 0.195$	$\mu^* = 0.15-0.1$	$\mu^* = 0.15-0.1$
λ	1.714	1.714	1.10	0.89
ω_{\log} , K	1333	1333	1082	695
ω_2 , K	1671	1671	1567	1287
α	0.46–0.48	0.43	0.44–0.48	0.42–0.47
T_c (A–D), K	168–198	149	74–94	32–43
T_c (E), K	236–247	226	90–115	36–46
$N(E_F)$, states/eV/f.u.	0.71	0.71	0.475	0.07
T_c (YD _x), K	168–176	168	54–67	22.4–32
$\Delta(0)$, meV	50–54	48	16–21	5–7.2
$\mu_0 H_C(0)$, T	63–66	60	16–21	1.9–2.7
$\Delta C/T_c$, mJ/mol·K ²	26.6–26.8	26.3	10.1–11.3	1.1–1.2
γ , mJ/mol·K ²	9.075	9.1	4.7	0.62
$R_\Delta = 2\Delta(0)/k_B T_c$	4.96–5.03	4.9	4.1–4.3	3.74–3.88

^a $60\times 60\times 60$ k -grid, $6\times 6\times 6$ q -grid and anharmonic $\alpha^2 F(\omega)$ were used; the harmonic approach gives $T_c = 272$ K (Table S8).

Table S8. Numerical solution of the Migdal–Eliashberg equations for harmonic and anharmonic $\alpha^2 F(\omega)$ of YH₆ at 165 GPa for different values of the Coloumb pseudopotential.

Coulomb pseudopotential μ^*	0	0.1	0.13	0.15	0.195
T_c , K (anharmonic)	269 ^a	247	240	236	226 ^a
T_c , K (harmonic)	294 ^a	272	265	261	251 ^a

^aLinear extrapolation.

Table S9. Additional electronic and superconducting parameters of YH₄ and YH₇ at $\mu^* = 0.15-0.1$ and YH₆ at $\mu^* = 0.195$ at the pressure of 165 GPa.

Parameter	$Im\bar{3}m$ -YH ₆	$I4/mmm$ -YH ₄	$Imm2$ -YH ₇
$N(E_F)$, states/eV/f.u.	0.71	0.475	0.07
Average Fermi velocity V_F , ^a m/s	5.3×10^5	$3.4-4.0\times 10^5$	$3.1-3.8\times 10^5$
London penetration depth λ_L , nm	93	180–141	208–155
Coherence length, Å	23	45–40	130–110
Ginzburg–Landau parameter κ	40	40–35	16–14.2
Lower critical magnetic field $\mu_0 H_{C1}$, mT	50	13–21	7.5–13
Upper critical field $\mu_0 H_{C2}$, T	60	16–21	2.7
Clogston–Chandrasekhar paramagnetic limit, T	582	193–260	61–88
Maximum critical current density (J_c , A/cm ²)	8.6×10^8	$1.2-2.2\times 10^8$	$3-6.5\times 10^7$

^aAccording to formula (S10)

The critical current density $J_c = en_e V_L$, evaluated using the Landau criterion for superfluidity,⁴⁸ $V_L = \min \frac{\varepsilon(p)}{p} \cong \frac{\Delta_0}{\hbar k_F}$, is around 10^9 A/cm² for YH₆, much higher than in H₃S.⁴⁹

Equations for calculating T_C and related parameters

To calculate the isotopic coefficient β , the Allen–Dynes interpolation formulas were used:

$$\beta_{\text{McM}} = -\frac{d\ln T_C}{d\ln M} = \frac{1}{2} \left[1 - \frac{1.04(1 + \lambda)(1 + 0.62\lambda)}{[\lambda - \mu^*(1 + 0.62\lambda)]^2} \mu^{*2} \right] \quad (\text{S2})$$

$$\beta_{\text{AD}} = \beta_{\text{McM}} - \frac{2.34\mu^{*2}\lambda^{3/2}}{(2.46 + 9.25\mu^*) \cdot ((2.46 + 9.25\mu^*)^{3/2} + \lambda^{3/2})} - \frac{130.4 \cdot \mu^{*2} \lambda^2 (1 + 6.3\mu^*) \left(1 - \frac{\omega_{\log}}{\omega_2} \right) \frac{\omega_{\log}}{\omega_2}}{\left(8.28 + 104\mu^* + 329\mu^{*2} + 2.5 \cdot \lambda^2 \frac{\omega_{\log}}{\omega_2} \right) \cdot \left(8.28 + 104\mu^* + 329\mu^{*2} + 2.5 \cdot \lambda^2 \left(\frac{\omega_{\log}}{\omega_2} \right)^2 \right)} \quad (\text{S3})$$

where the last two correction terms are usually small (~ 0.01).

The Sommerfeld constant was found as

$$\gamma = \frac{2}{3} \pi^2 k_B^2 N(E_F) (1 + \lambda) \quad (\text{S4})$$

and was applied to estimate the upper critical magnetic field and the superconductive gap in yttrium hydrides by well-known semiempirical equations of the BCS theory (Ref. ⁵⁰, Equations 4.1 and 5.11), which can be used for $T_C/\omega_{\log} < 0.25$:

$$\frac{\gamma T_C^2}{B_{C2}^2(0)} = 0.168 \left[1 - 12.2 \left(\frac{T_C}{\omega_{\log}} \right)^2 \ln \left(\frac{\omega_{\log}}{3T_C} \right) \right] \quad (\text{S5})$$

$$\frac{2\Delta(0)}{k_B T_C} = 3.53 \left[1 + 12.5 \left(\frac{T_C}{\omega_{\log}} \right)^2 \ln \left(\frac{\omega_{\log}}{2T_C} \right) \right] \quad (\text{S6})$$

The lower critical magnetic field was calculated according to the Ginzburg–Landau theory:⁴⁷

$$\frac{H_{C1}}{H_{C2}} = \frac{\ln k}{2\sqrt{2}k^2}, k = \lambda_L/\xi, \quad (\text{S7})$$

where λ_L is the London penetration depth:

$$\lambda_L = 1.0541 \times 10^{-5} \sqrt{\frac{m_e c^2}{4\pi n_e e^2}}. \quad (\text{S8})$$

Here c is the speed of light, e is the electron charge, m_e is the electron mass, and n_e is an effective concentration of charge carriers, evaluated from the average Fermi velocity (V_F) in the Fermi gas model:

$$n_e = \frac{1}{e\pi^2} \left(\frac{m_e V_F}{\hbar} \right)^3. \quad (\text{S9})$$

The coherence length ξ was found as $\xi = \sqrt{\hbar/2e(\mu_0 H_{C2})}$ and was used to estimate the average Fermi velocity:

$$V_F = \frac{\pi\Delta(0)}{\hbar}\xi. \quad (\text{S10})$$

The average Fermi velocity was also calculated directly from the band structure of *cI4*-YH₆ using

$$\langle V_F \rangle = \sqrt{\frac{\sum_k \delta(E_k - E_F) V_k^2}{\sum_k \delta(E_k - E_F)}} = \frac{a}{\pi\hbar} \sqrt{\frac{\sum_k \delta(E_k - E_F) (dE_k/dt)^2}{\sum_k \delta(E_k - E_F)}}. \quad (\text{S11})$$

where dE_i/dk ($k = -\pi/a \dots \pi/a$) were replaced by dE_i/dt ($t = -1 \dots 1$). In this case the first Brillouin zone was sampled by the very dense k -points mesh with a resolution of $2\pi \times 0.005 \text{ \AA}^{-1}$. The obtained values of V_F of YH₆ are 9.1×10^5 , 9.3×10^5 and 9.4×10^5 m/s at 150, 165, and 180 GPa, respectively.

Electron band mass was found to be $m^* = 0.82m_e$ for YH₆ at 150 GPa ($0.69m_e$ in the vicinity of the Γ -point), which is compatible the electron band mass in H₃S⁵¹.

The calculations within the Migdal–Eliashberg approach were made using the following equations (on the imaginary axis):²⁹

$$\Delta_n = \frac{\pi}{\beta} \sum_{m=-Max}^{Max} \frac{\lambda(i\omega_n - i\omega_m) - \mu^* \theta(\omega_c - |\omega_m|)}{\sqrt{\omega_m^2 Z_m^2 + \Delta_m^2}} \Delta_m. \quad (\text{S12})$$

$$Z_n = 1 + \frac{\pi}{\beta\omega_n} \sum_{m=-Max}^{Max} \frac{\lambda(i\omega_n - i\omega_m)}{\sqrt{\omega_m^2 Z_m^2 + \Delta_m^2}} \omega_m Z_m. \quad (\text{S13})$$

$$\lambda(z) = \int_0^{\omega_c} \frac{2\alpha^2 F(\omega)}{\omega^2 - z^2} \omega d\omega. \quad (\text{S14})$$

where Δ_n is the order parameter function, Z_n is the wave function renormalization factor, $\theta(x)$ is the Heaviside function, $\omega_n = \pi k_B T (2n - 1)$ is the n th Matsubara frequency, $\beta = k_B T$, μ^* is the Coulomb pseudopotential, $\lambda(z)$ is the electron–phonon pairing kernel, and ω_c is the cutoff energy. We used $\omega_c = 6 \text{ Ry}$ with the appropriate number of the Matsubara frequencies.

Electronic and phonon properties of yttrium hydrides

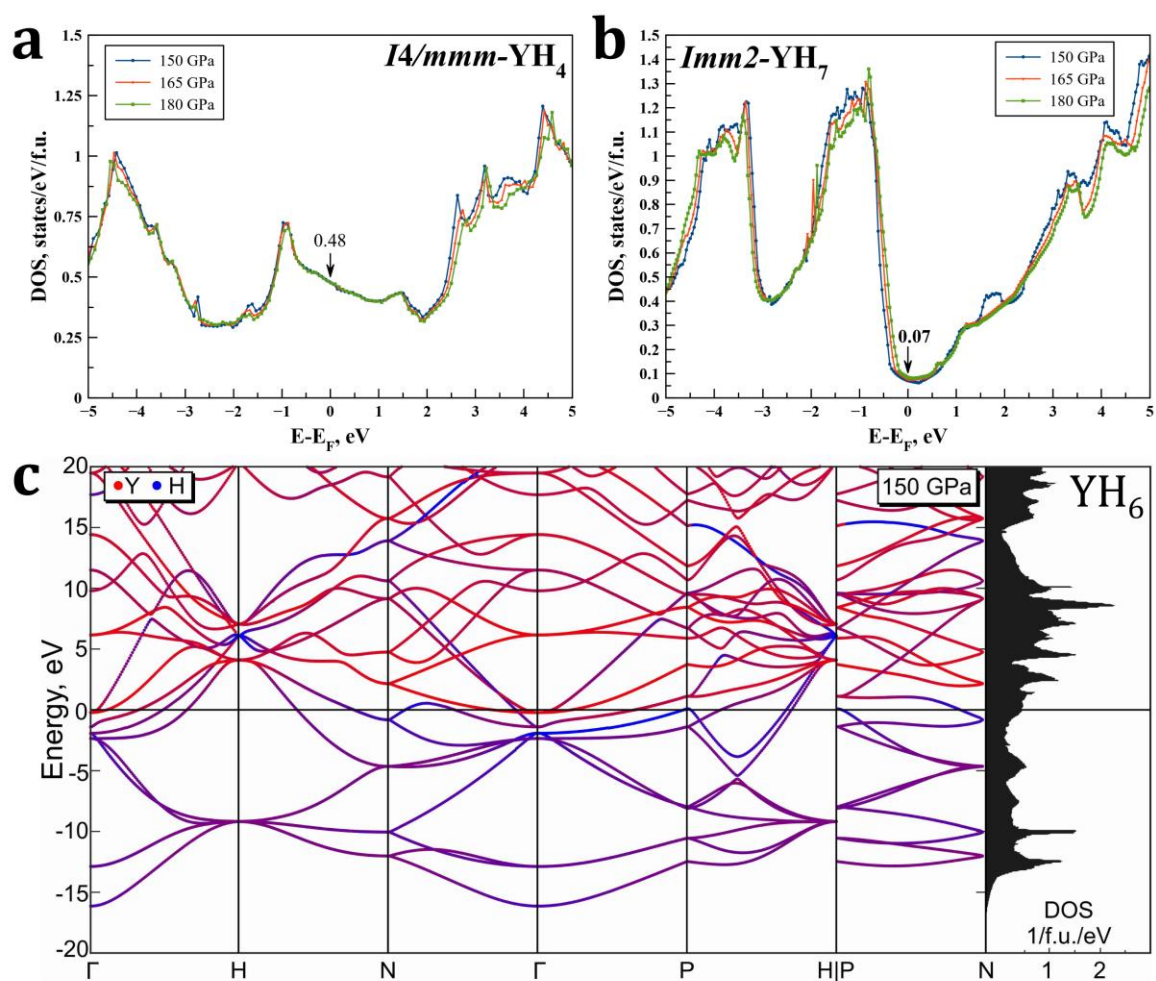


Figure S17. Electronic properties of yttrium hydrides: (a) density of electronic states of $I4/mmm\text{-YH}_4$ at E_F ; (b) density of electronic states of $Imm2\text{-YH}_7$ at E_F ; (c) band structure of $cI4\text{-YH}_6$ at 150 GPa.

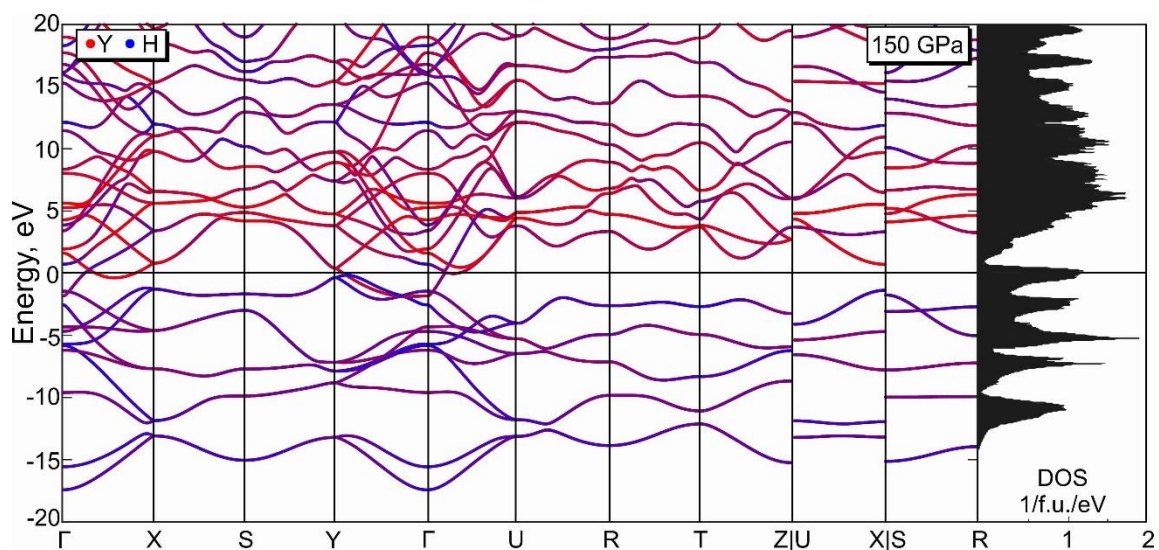


Figure S18. Electronic density of states and band structure of $Imm2\text{-YH}_7$ at 150 GPa.

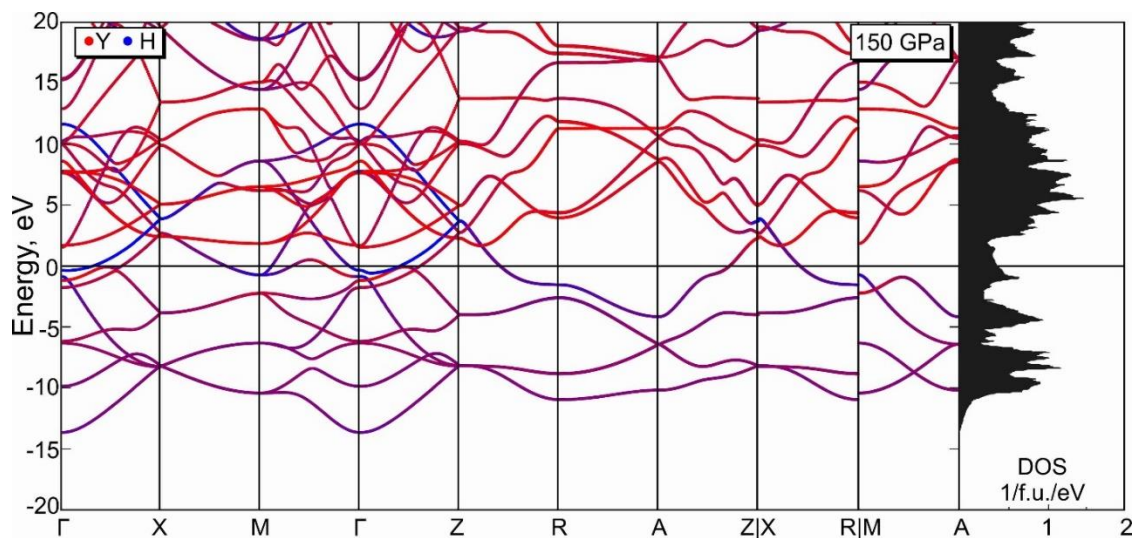


Figure S19. Electronic density of states and band structure of $I4/mmm$ -YH₄ at 150 GPa.

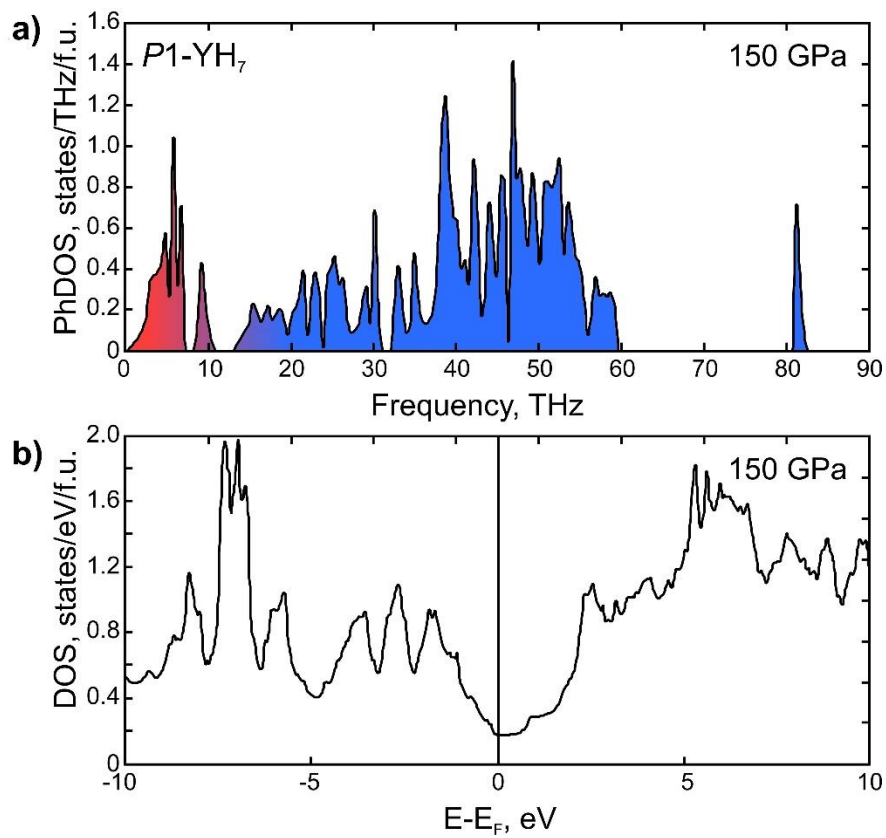


Figure S20. (a) Harmonic phonon density of states and (b) electronic density of states of $P1$ -YH₇ at 150 GPa.

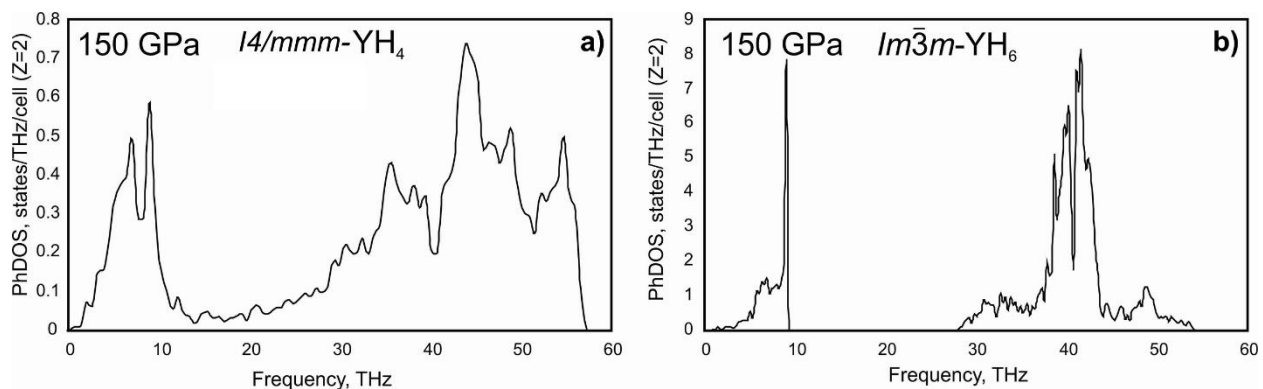


Figure S21. Harmonic phonon density of states of (a) YH_4 and (b) YH_6 at 150 GPa.

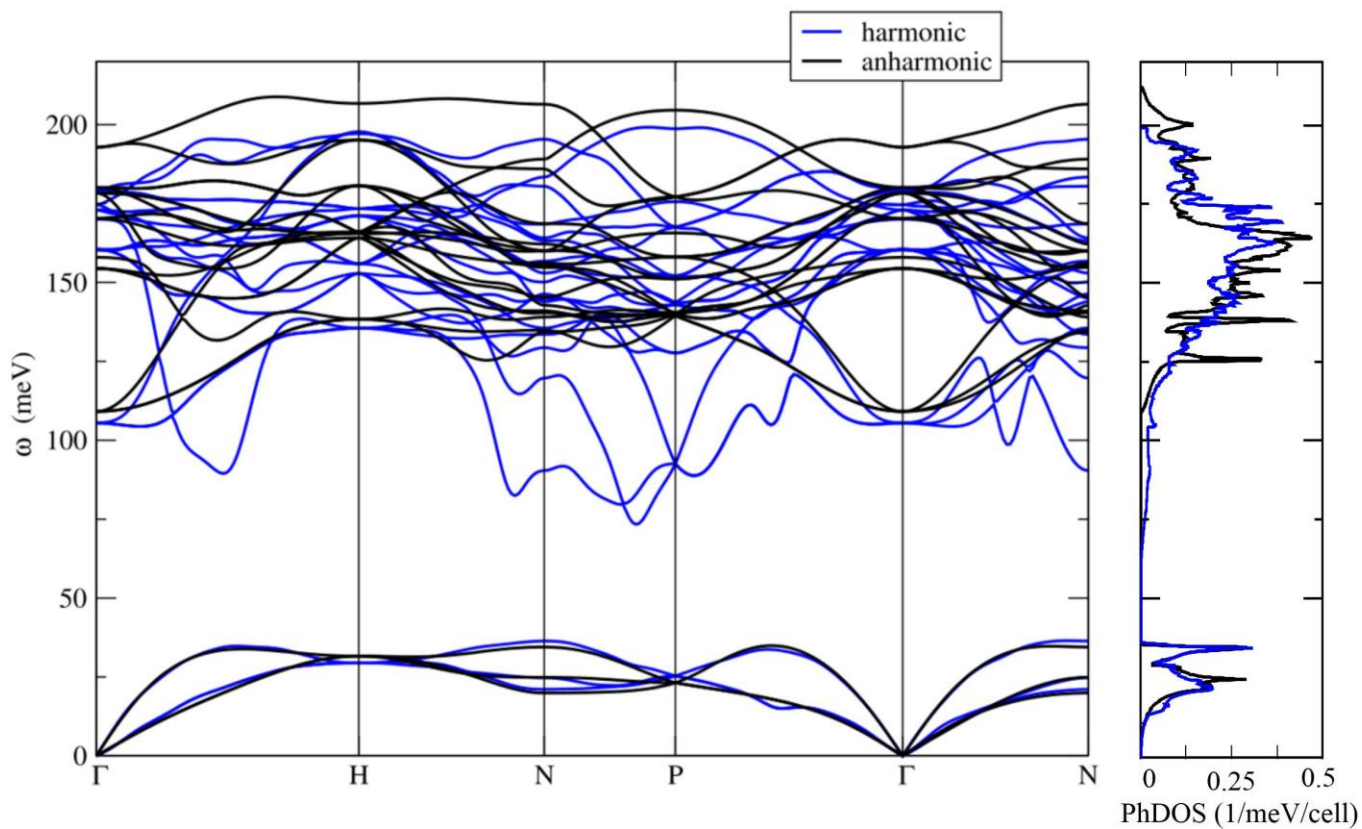


Figure S22. Harmonic (blue) and anharmonic (black) phonon band structure and density of states of $\text{Im}\bar{3}m\text{-YH}_6$ at 165 GPa.

Elastic properties of Y–H phases

The elastic tensors of YH₄, YH₆ and YH₇ were calculated using the stress-strain relations:

$$C_{ij} = \frac{\partial \sigma_i}{\partial \eta_j}, \quad (\text{S15})$$

where σ_i is the i^{th} component of the stress tensor, η_j is the j^{th} component of the strain tensor.

The bulk (B) and shear (G) moduli and Young's modulus (E) were calculated in GPa via Voigt-Reuss-Hill averaging.^{52,53} Using obtained values of elastic moduli, we calculated the velocities of longitudinal and transverse acoustic waves:

$$v_{LA} = \sqrt{\frac{C_{11}}{\rho}}, \quad v_{TA} = \sqrt{\frac{C_{11}-C_{12}}{2\rho}}, \quad (\text{S16})$$

where C_{11} , C_{12} are elastic constants, ρ is a density of compound. Obtained values allow us to estimate Debye temperature as⁵⁴:

$$\theta_D = \frac{h}{k_B} \left[\frac{3n}{4\pi} \left(\frac{N_A \cdot \rho}{M} \right) \right]^{\frac{1}{3}} v_m, \quad (\text{S17})$$

where h , k_B , N_A are Planck's, Boltzmann's and Avogadro constants, v_m is an average velocity of acoustic waves calculated by the following formula

$$v_m = \left[\frac{1}{3} \left(\frac{2}{v_{TA}^3} + \frac{1}{v_{LA}^3} \right) \right]^{-1/3}. \quad (\text{S18})$$

Table S10. Elastic and thermodynamic parameters of $Im\bar{3}m$ -YH₆ ($Z = 2$).

Parameter	150 GPa	165 GPa	180 GPa
a , Å	3.602	3.573	3.546
V_{DFT} , Å ³	46.73	45.61	44.59
C_{11} , GPa	637	870	980
C_{12} , GPa	435	460	482
C_{44} , GPa	109	196	283
B , GPa	569	597	648
G , GPa	109	196	283
E , GPa	307	593	705
B/G	5.22	3.04	2.28
Poisson's ratio η	0.410	0.352	0.308
Density ρ , kg/m ³	6744	6910	7069
Transverse sound velocity v_t , m/s	4019	5326	6354
Longitudinal sound velocity v_l , m/s	10291	11145	12062
Debye temperature θ_D , K	908	1204	1438

Table S11. Elastic and thermodynamic parameters of $I4/mmm$ -YH₄ ($Z = 2$).

Parameter	150 GPa	165 GPa	180 GPa
a , Å	2.779	2.752	2.724
c , Å	5.277	5.259	5.236
V_{DFT} , Å ³	40.758	39.829	38.866
C_{11} , GPa	800	813	856
C_{12} , GPa	425	406	361
C_{13} , GPa	480	508	607
C_{33} , GPa	1014	1082	1035
C_{44} , GPa	229	234	167
C_{66} , GPa	207	233	218
B , GPa	592	601	631
G , GPa	214	209	183
E , GPa	573	562	501
B/G	2.768	2.876	3.449
Poisson's ratio η	0.338	0.344	0.367
Density ρ , kg/m ³	7570	7747	7939
Transverse sound velocity v_t , m/s	5330	5197	4816
Longitudinal sound velocity v_l , m/s	10774	10658	10508
Debye temperature θ_D , K	1115	1097	1028

Table S12. Elastic and thermodynamic parameters of $Imm2$ -YH₇ ($Z = 2$).

Parameter	150 GPa	165 GPa	180 GPa
a , Å	3.281	3.258	3.235
b , Å	3.402	3.369	3.340
c , Å	4.676	4.632	4.590
V_{DFT} , Å ³	52.19	50.85	49.59
C_{11} , GPa	821	847	910
C_{12} , GPa	369	374	436
C_{13} , GPa	480	505	559
C_{22} , GPa	896	923	958
C_{23} , GPa	310	334	351
C_{33} , GPa	840	881	926
C_{44} , GPa	138	140	142
C_{55} , GPa	122	136	143
C_{66} , GPa	328	407	425
B , GPa	541	563	608
G , GPa	195	212	218
E , GPa	523	566	583
B/G	2.766	2.649	2.793
Poisson ratio η	0.338	0.332	0.340
Density ρ , kg/m ³	5920	6075	6228
Transverse sound velocity v_t , m/s	5760	5920	5113
Longitudinal sound velocity v_l , m/s	11650	11810	12010
Debye temperature θ_D , K	1300	1345	1356

References

1. Prescher, C. & Prakapenka, V. B. DIOPTAS: a program for reduction of two-dimensional X-ray diffraction data and data exploration. *High Pressure Research* **35**, 223–230 (2015).
2. Petříček, V., Dušek, M. & Palatinus, L. Crystallographic Computing System JANA2006: General features. *Zeitschrift für Kristallographie - Crystalline Materials* **229**, 345–352 (2014).
3. Bail, A. L. Whole powder pattern decomposition methods and applications: A retrospection. *Powder Diffraction* **20**, 316–326 (2005).
4. Prakapenka, V. B. *et al.* Advanced flat top laser heating system for high pressure research at GSECARS: application to the melting behavior of germanium. *High Pressure Research* **28**, 225–235 (2008).
5. Akahama, Y. & Kawamura, H. Pressure calibration of diamond anvil Raman gauge to 410 GPa. *J. Phys.: Conf. Ser.* **215**, 012195 (2010).
6. Holtgrewe, N., Greenberg, E., Prescher, C., Prakapenka, V. B. & Goncharov, A. F. Advanced integrated optical spectroscopy system for diamond anvil cell studies at GSECARS. *High Pressure Research* **39**, 457–470 (2019).
7. Eremets, M. I. Megabar high-pressure cells for Raman measurements. *Journal of Raman Spectroscopy* **34**, 515–518 (2003).
8. Parvanov, V. M. *et al.* Materials for hydrogen storage: structure and dynamics of borane ammonia complex. *Dalton Trans.* 4514–4522 (2008) doi:10.1039/B718138H.
9. Dew-Hughes, D. Flux pinning mechanisms in type II superconductors. *The Philosophical Magazine: A Journal of Theoretical Experimental and Applied Physics* **30**, 293–305 (1974).
10. Oganov, A. R. & Glass, C. W. Crystal structure prediction using ab initio evolutionary techniques: Principles and applications. *J. Chem. Phys.* **124**, 244704 (2006).
11. Oganov, A. R., Lyakhov, A. O. & Valle, M. How Evolutionary Crystal Structure Prediction Works—and Why. *Acc. Chem. Res.* **44**, 227–237 (2011).
12. Lyakhov, A. O., Oganov, A. R., Stokes, H. T. & Zhu, Q. New developments in evolutionary structure prediction algorithm USPEX. *Computer Physics Communications* **184**, 1172–1182 (2013).
13. Bushlanov, P. V., Blatov, V. A. & Oganov, A. R. Topology-based crystal structure generator. *Computer Physics Communications* **236**, 1–7 (2019).
14. Hohenberg, P. & Kohn, W. Inhomogeneous electron gas. *Phys Rev* **136**, B864–B871 (1964).
15. Kohn, W. & Sham, L. J. Self-consistent equations including exchange and correlation effects. *Phys Rev* **140**, A1133–A1138 (1965).
16. Perdew, J. P., Burke, K. & Ernzerhof, M. Generalized gradient approximation made simple. *Physical review letters* **77**, 3865–3868 (1996).
17. Blöchl, P. E. Projector augmented-wave method. *Phys. Rev. B* **50**, 17953–17979 (1994).
18. Kresse, G. & Joubert, D. From ultrasoft pseudopotentials to the projector augmented-wave method. *Phys. Rev. B* **59**, 1758–1775 (1999).
19. Kresse, G. & Furthmüller, J. Efficient iterative schemes for ab initio total-energy calculations using a plane-wave basis set. *Phys. Rev. B* **54**, 11169–11186 (1996).
20. Kresse, G. & Hafner, J. Ab initio molecular dynamics for liquid metals. *Phys. Rev. B* **47**, 558–561 (1993).
21. Kresse, G. & Hafner, J. Ab initio molecular-dynamics simulation of the liquid-metal amorphous-semiconductor transition in germanium. *Phys. Rev. B* **49**, 14251–14269 (1994).
22. Semenok, D. V., Kvashnin, A. G., Kruglov, I. A. & Oganov, A. R. Actinium Hydrides AcH₁₀, AcH₁₂, and AcH₁₆ as High-Temperature Conventional Superconductors. *J. Phys. Chem. Lett.* **9**, 1920–1926 (2018).

23. Kvashnin, A. G., Semenov, D. V., Kruglov, I. A., Wrona, I. A. & Oganov, A. R. High-Temperature Superconductivity in Th-H System at Pressure Conditions. *ACS Applied Materials & Interfaces* **10**, 43809–43816 (2018).
24. Togo, A. & Tanaka, I. First principles phonon calculations in materials science. *Scripta Materialia* **108**, 1–5 (2015).
25. Togo, A., Oba, F. & Tanaka, I. First-principles calculations of the ferroelastic transition between rutile-type and CaCl₂-type SiO₂ at high pressures. *Phys. Rev. B* **78**, 134106 (2008).
26. Giannozzi, P. *et al.* QUANTUM ESPRESSO: a Modular and Open-Source Software Project for Quantum Simulations of Materials. *Journal of Physics: Condensed Matter* **21**, 395502 (2009).
27. Giannozzi, P. *et al.* Advanced capabilities for materials modelling with Quantum ESPRESSO. *J. Phys.: Condens. Matter* **29**, 465901 (2017).
28. Baroni, S., de Gironcoli, S., Dal Corso, A. & Giannozzi, P. Phonons and Related Crystal Properties from Density-Functional Perturbation Theory. *Reviews of modern Physics* **73**, 515–562 (2001).
29. Eliashberg, G. M. Interactions between Electrons and Lattice Vibrations in a Superconductor. *JETP* **11**, 696–702 (1959).
30. Allen, P. B. & Dynes, R. C. Transition temperature of strong-coupled superconductors reanalyzed. *Phys. Rev. B* **12**, 905–922 (1975).
31. Lüders, M. *et al.* Ab initio theory of superconductivity. I. Density functional formalism and approximate functionals. *Phys. Rev. B* **72**, 024545 (2005).
32. Marques, M. A. L. *et al.* Ab initio theory of superconductivity. II. Application to elemental metals. *Phys. Rev. B* **72**, 024546 (2005).
33. Kruglov, I. A. *et al.* Superconductivity of LaH₁₀ and LaH₁₆ polyhydrides. *Phys. Rev. B* **101**, 024508 (2020).
34. Akashi, R. & Arita, R. Density functional theory for superconductors with particle-hole asymmetric electronic structure. *Phys. Rev. B* **88**, 014514 (2013).
35. Akashi, R., Kawamura, M., Tsuneyuki, S., Nomura, Y. & Arita, R. First-principles study of the pressure and crystal-structure dependences of the superconducting transition temperature in compressed sulfur hydrides. *Phys. Rev. B* **91**, 224513 (2015).
36. Migdal, A. B. Interaction between electrons and lattice vibrations in a normal metal. *JETP* **34**, 996–1001 (1958).
37. Scalapino, D. J. The Electron Phonon Interaction and Strong Coupling. in *Superconductivity: Part 1 (In Two Parts)* (ed. Parks, R. D.) vol. 1 (Dekker, New York, 1969).
38. Schrieffer, J. R. *Theory Of Superconductivity*. vol. 1 (Perseus Books, 1999).
39. Pines, D. *Elementary Excitations in Solids : Lectures on Phonons, Electrons, and Plasmons*. (Perseus, 1999).
40. Rath, J. & Freeman, A. J. Generalized magnetic susceptibilities in metals: Application of the analytic tetrahedron linear energy method to Sc. *Phys. Rev. B* **11**, 2109–2117 (1975).
41. Errea, I., Calandra, M. & Mauri, F. Anharmonic free energies and phonon dispersions from the stochastic self-consistent harmonic approximation: Application to platinum and palladium hydrides. *Phys. Rev. B* **89**, 064302 (2014).
42. Grishakov, K. S., Degtyarenko, N. N. & Mazur, E. A. Electron, Phonon, and Superconducting Properties of Yttrium and Sulfur Hydrides under High Pressures. *J. Exp. Theor. Phys.* **128**, 105–114 (2019).
43. Heil, C., di Cataldo, S., Bachelet, G. B. & Boeri, L. Superconductivity in sodalite-like yttrium hydride clathrates. *Phys. Rev. B* **99**, 220502 (2019).
44. Li, Y. *et al.* Pressure-stabilized superconductive yttrium hydrides. *Scientific Reports* **5**, 09948 (2015).
45. Liu, H., Naumov, I. I., Hoffmann, R., Ashcroft, N. W. & Hemley, R. J. Potential high-T_c superconducting lanthanum and yttrium hydrides at high pressure. *PNAS* **114**, 6990–6995 (2017).

46. Bergara, A. Anharmonic effects and optical spectra in superconducting hydrogen. in *Proceedings of 56th EHPRG Meeting* (2018).
47. Ginzburg, V. L. & Landau, L. D. On the Theory of superconductivity. *Zh.Eksp.Teor.Fiz.* **20**, 1064–1082 (1950).
48. Landau, L. Theory of the Superfluidity of Helium II. *Phys. Rev.* **60**, 356–358 (1941).
49. Drozdov, A. P., Eremets, M. I., Troyan, I. A., Ksenofontov, V. & Shylin, S. I. Conventional superconductivity at 203 kelvin at high pressures in the sulfur hydride system. *Nature* **525**, 73–76 (2015).
50. Carbotte, J. P. Properties of boson-exchange superconductors. *Rev. Mod. Phys.* **62**, 1027–1157 (1990).
51. Quan, Y. & Pickett, W. E. Van Hove singularities and spectral smearing in high-temperature superconducting H3S. *Phys. Rev. B* **93**, 104526 (2016).
52. Hill, R. The Elastic Behaviour of a Crystalline Aggregate. *Proc. Phys. Soc. A* **65**, 349 (1952).
53. Anderson, O. L. A simplified method for calculating the debye temperature from elastic constants. *Journal of Physics and Chemistry of Solids* **24**, 909–917 (1963).
54. Ravindran, P. *et al.* Density functional theory for calculation of elastic properties of orthorhombic crystals: Application to TiSi2. *Journal of Applied Physics* **84**, 4891–4904 (1998).